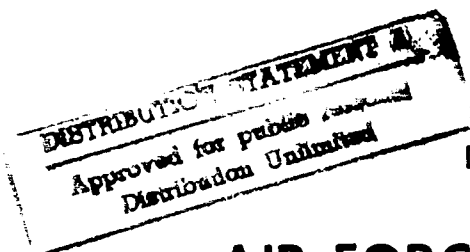GENERATION OF A SINGLE-LOBE, FAR-FIELD
INTENSITY PATTERN FROM A LASER DIODE
ARRAY USING AN OPTICAL DELAY LINE

THESIS

Thomas A. Summers, Captain, USAF
AFIT/GAP/ENP/94D-10

DEPARTMENT OF THE AIR FORCE

AIR UNIVERSITY

AIR FORCE INSTITUTE OF TECHNOLOGY

19941228 028

Wright-Patterson Air Force Base, Ohio

AFIT/GAP/ENP/94D-10

GENERATION OF A SINGLE-LOBE, FAR-FIELD
INTENSITY PATTERN FROM A LASER DIODE
ARRAY USING AN OPTICAL DELAY LINE

THESIS

Thomas A. Summers, Captain, USAF
AFIT/GAP/ENP/94D-10

DTIC QUALITY INSPECTED 2

REPORT DOCUMENTATION PAGE

1. AGENCY USE ONLY (Leave blank)	2. REPORT DATE December 1994	3. REPORT TYPE AND DATES COVERED Master's Thesis

4. TITLE AND SUBTITLE

GENERATION OF A SINGLE-LOBE, FAR-FIELD INTENSITY PATTERN FROM A LASER DIODE ARRAY USING AN OPTICAL DELAY LINE

5. FUNDING NUMBERS

6. AUTHOR(S)

Thomas A. Summers, Captain, USAF

7. PERFORMING ORGANIZATION NAME(S) AND ADDRESS(ES)

Air Force Institute of Technology
2750 P Street
Wright-Patterson AFB OH 45433-6583

8. PERFORMING ORGANIZATION REPORT NUMBER

AFIT/GAP/ENP/94D-10

9. SPONSORING/MONITORING AGENCY NAME(S) AND ADDRESS(ES)

The Philips Laboratory (PL/LIDA)
3550 Aberdeen AVE, SE
Kirtland AFB NM 87117

10. SPONSORING/MONITORING AGENCY REPORT NUMBER

11. SUPPLEMENTARY NOTES

12a. DISTRIBUTION/AVAILABILITY STATEMENT

Approved for public release; distribution unlimited.

12b. DISTRIBUTION CODE

13. ABSTRACT (Maximum 200 words)

A simple and practical technique is demonstrated to generate a stable, single-lobe, far-field intensity pattern from a one-dimensional, antiphased, laser diode array with gain-guided elements. The two far-field lobes of the array are combined after introducing an optical delay line into the path of one of the lobes to make the lobes mutually incoherent. The incoherent superposition of intensities produces a near-diffraction-limited, single-lobe, far-field intensity pattern containing 84% of the power, exceeding any previous (known) phase control experiments. This technique compares favorably with more elaborate schemes advanced previously using integrated phase plates, etc. The method is directly applicable to one-dimensional laser diode arrays and could be adapted for use with two-dimensional arrays as well.

14. SUBJECT TERMS

Semiconductor Lasers, Infrared Lasers, Laser Diode Arrays, Optical Delay Line, Laser Applications

15. NUMBER OF PAGES

94

16. PRICE CODE

17. SECURITY CLASSIFICATION OF REPORT	18. SECURITY CLASSIFICATION OF THIS PAGE	19. SECURITY CLASSIFICATION OF ABSTRACT	20. LIMITATION OF ABSTRACT
Unclassified	Unclassified	Unclassified	UL

AFIT/GAP/ENP/94D-10

GENERATION OF A SINGLE-LOBE, FAR-FIELD

INTENSITY PATTERN FROM A LASER DIODE ARRAY

USING AN OPTICAL DELAY LINE

THESIS

Presented to the Faculty of the School of Engineering

of the Air Force Institute of Technology

Air University

In Partial Fulfillment of the

Requirements for the Degree of

Master of Science in Engineering Physics

Thomas A. Summers, B.S.

Captain, USAF

December 1994

Approved for public release; distribution unlimited

Acknowledgments

Table of Contents

List of Figures

Abstract

A simple and practical technique is demonstrated to generate a stable, single-lobe, far-field intensity pattern from a one-dimensional, antiphased, laser diode array with gain-guided elements. The two far-field lobes of the array are combined after introducing an optical delay line into the path of one of the lobes to make the lobes mutually incoherent. The incoherent superposition of intensities produces a near-diffraction-limited, single-lobe, far-field intensity pattern containing 84% of the power, exceeding any previous (known) phase control experiments. This technique compares favorably with more elaborate schemes advanced previously using integrated phase plates, etc. The method is directly applicable to one-dimensional laser diode arrays and could be adapted for use with two-dimensional arrays as well.

GENERATION OF A SINGLE-LOBE, FAR-FIELD INTENSITY PATTERN FROM A LASER DIODE ARRAY USING AN OPTICAL DELAY LINE

I. Introduction

Background and Previous Work

Many military and commercial applications would benefit from inexpensive, durable, versatile, compact, light-weight, long lifetime, high power, efficient lasers. This laser could apply to and enhance many military missions, but would be especially useful for the United States Air Force (U.S.A.F.) in meeting its mission to defend the United States through control and exploitation of air and space. Proposed applications include free-space communication,[1] airborne Doppler laser radar, ground-based laser radar, biological warfare/chemical warfare (BW/CW)-agent detection, environmental control,[2] ordinance initiation, fuses, electro-optic countermeasures, laser blinding, infrared (IR) aiming lights, IR pointing and tracking, target designators, range finders and altimeters, range image sensors, obstacle avoidance, and battlefield medical applications.[3, 4] While such a laser would obviously meet a variety of critical military needs, commercial

industry and society would also profit from such a device. Some commercial applications include fiber-optic information transmission, optical recording at high data rates, high-speed laser printers, compact-disc players,[5, 6] optical pumping of other lasers (i.e., neodymium-doped yttrium-aluminum-garnet, $Nd:Y_3Al_5O_{12}$ (Nd:YAG), lasers),[7] and laser power beaming systems.[8] Small laser diodes (LDs), semiconductor devices developed in the past few years that directly convert electrical into optical energy, appear perfectly suited to meet all these needs and have the potential to make this source of light as common as an electric light bulb.

Laser diodes show tremendous potential for military and commercial applications since they meet the requirements listed above, but they are limited in their maximum output power due to possible emitter facet (also called element) damage at high output densities.[9] The output power of single-element, edge-emitting LDs, as shown in Figure 1, can be increased by increasing either the size of or number of elements (or both). Unfortunately, it is nearly impossible to achieve stable, high-power laser operation by increasing the size of the elements due to uncontrollable transverse modes and filamentary oscillation that can destroy the device.[11] Fortunately, LDs can be made by adding elements (individual lasers), as shown in Figure 2, and result in LDs with multiple elements, known as laser diode arrays (LDAs). LDAs operate either coherently or incoherently. If the elements of a LDA are located close together on the diode chip so the evanescent (or surface) electric-field waves out of each gain section couple to nearest neighbors, the array is said to be phase-locked (coherent with one another) and the array
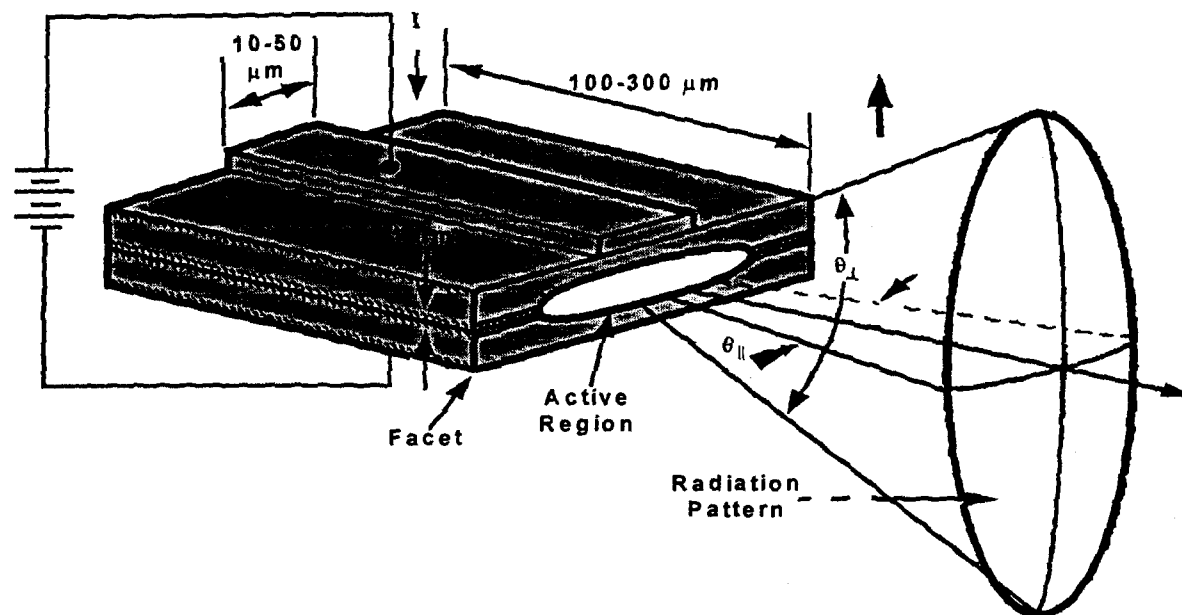
Figure 1. One-element, gain-guided laser diode. [From Reference 10]
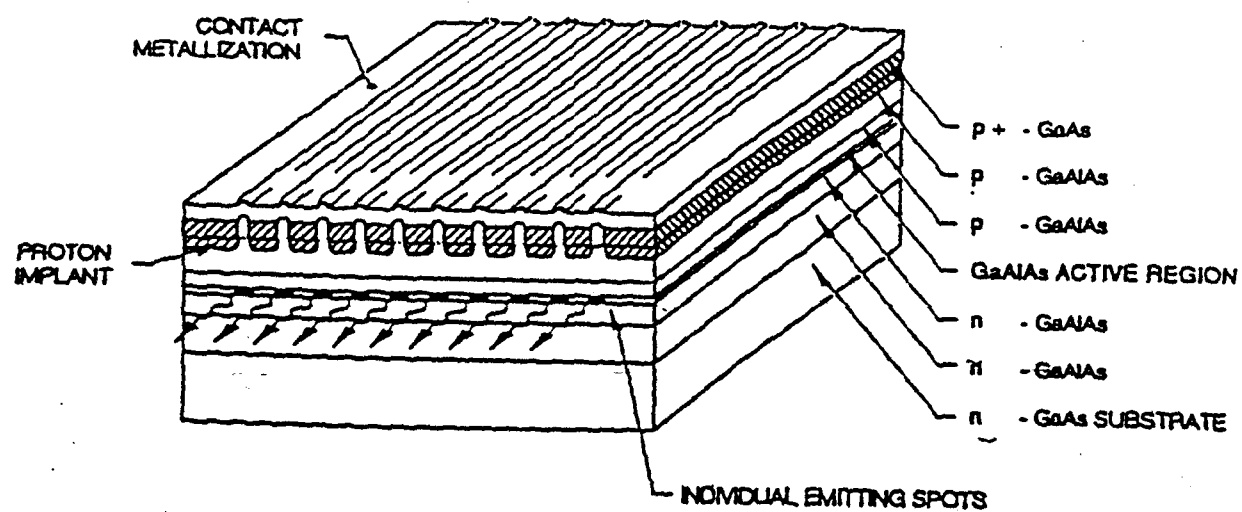
Figure 2. Monolithic, ten-element, gain-guided laser diode array. [From Reference 12]

operates coherently.[9] Several coherent LDA phase-locked modes are possible, but two cases are of particular interest: the in-phase mode (0 degree phase difference between adjacent elements) or out-of-phase mode (180 degree or π phase difference between adjacent elements).[13] If the elements couple in phase, the resulting observable intensity pattern is a single, ideally diffraction-limited (the ratio of the wavelength over the emitting aperture), narrow lobe (beam) in the far field. But, if on the other hand the elements of the LDA couple out-of-phase, the resulting observable far-field intensity pattern has two lobes. When no coupling occurs between adjacent elements, the LDA operates incoherently.

Phase-locked LDAs are usually found to operate coherently in the out-of-phase mode. This is because the laser itself selects the phase difference between elements so as to minimize its threshold current (the current needed for lasing to occur) and favors the out-of-phase mode.[14] Thus LDAs generally produce the two-lobe, far-field intensity pattern dividing the available energy into two primary lobes and some secondary lobes. However, for many applications, as stated above, it is desirable to have the maximum output power in a single-lobe, diffraction-limited far-field intensity pattern instead of a two-lobe pattern.

How can the U.S.A.F. and industry exploit the high output powers achievable with LDAs as well as get a single-lobe, near-diffraction-limited far-field intensity pattern? The answer is to either change the preferred out-of-phase difference mode of the LDA to an in-phase mode between elements or somehow combine the two-lobe far-field

4

intensity pattern into a single lobe. Zealous research using these approaches continues to try to produce a single-lobe intensity pattern with maximum output power.

In the Air Force's and industry's quest for high output powers from LDs and LDAs, one major research approach has been to use one-dimensional (monolithic) arrays of mutually coupled (phase-locked) laser diodes as shown in Figure 2. While semiconductor gain-guided (devices where the injection-carrier profile provides the lateral optical-mode confinement), single-element LDs can produce maximum continuous wave (CW) output powers of around 4 W, multi-element LDAs can operate with reported maximum output powers of up to 20 W CW.[5]

Several experiments have demonstrated and some people have proposed procedures for the creation of diffraction-limited, single-lobe intensity patterns in the far-field using multi-element LDAs. Most recent research has centered on attempts to control the phasing between the elements in the near field of the LDAs.

One approach allows the LDA to operate in the out-of-phase mode and then rectifies the near-field electric-field using phase shifters. Fixed phase shifters, either near contact or integrated with the array, are made by etching patterns into a semiconducting material and relying on the index of refraction difference between air and the material to create an index grating. For example, Thaniyavarn and Dougherty used a very simple and practical technique to generate a single-lobe, far-field pattern from an LDA by placing a variable phase-shift zone plate near the laser output facet to readjust the phase distribution of the array into an all-in-phase distribution.[15] Using the integrated phase

shifter idea, Ackley *et al.* suggested using $\lambda/2$ Al_2O_3 selective coatings fabricated on uncoated or $\lambda/2$-coated array elements to form a new type of phase-locked laser array with an internal, integrated phase shifter to produce the desired single-lobe, diffraction-limited output beam.[16] Similar to this phase shifter approach, Matsumoto *et al.* showed a diffraction-limited, single-lobe, far-field intensity pattern could be made by placing a phase corrector plate at the image of the array elements.[17] The phase corrector plate, consisting of a Al_2O_3 facet coating with a different film thickness on each array element, acted as a phase shifter to convert the out-of-phase mode into an in-phase mode to produce a stable single-lobe, far-field pattern. Theoretically, the desired operating mode with 0 degree phase shift between all array elements can be achieved by varying the optical path length of the phase shifters. Experimentally, a variable external phase shifter can be made using an amplifier with several elements as shown by Itoh *et al.* They varied the injection current to individual elements, thus changing the index of refraction and the phase shift of each element.[18] Recently Kenyon tried to modify the liquid crystal display from an inexpensive pocket television into a spatial light modulator for the purpose of altering the phase front of a LDA to produce the desired single-lobe, far-field pattern, but nonuniformities in the phase shifter and insufficient phase shift prevented success.[19]

Another group, Welch *et al.*, reported pulsed outputs of up to 575 mW in a single-lobe, far-field pattern by offsetting two stripe (element) regions of the *p - n* junction of the laser structure from the stripes in the central region.[20] This caused the highest-order (two lobes) supermode to have a higher overlap with the gain profile and a lower lasing

threshold. This arrangement of stripes in the offset stripe laser equalized the gain along all paths in the cavity and tended to equalize the supermode gains creating a single-lobe, far-field pattern.

Two selective external feedback techniques have also been used to get a single lobe from LDAs: suppression of higher-order transverse array modes using spatial filtering within an external cavity and selective angular feedback to effectively self-injection lock the array operation. By placing a LDA in an external cavity and making use of the Talbot self-imaging effect to couple the laser diodes together, higher-order transverse array modes were suppressed using spatial filtering to get coherent laser operation.[21] Another method produced a near single-lobe, far-field pattern from coherent operation of an incoherent LDA and an external cavity.[22] Leger *et al.* produced a diffraction-limited, single-lobe, far-field pattern containing 82 percent of the total power when they used a diffractive microlens array to collimate the individual array elements to approximate a plane wave, and a diffractive coupling from an external cavity mirror to furnish mutual coherence. Using a novel approach of a graded index (GRIN) lens with a gold stripe mirror in an external cavity configuration, Chang-Hasnain *et al.* selectively fed back into the array one of the two lobes of a high-order supermode and took the other lobe as the output.[23] With this system they achieved high output power (700 mW) in a nearly diffraction-limited, single-lobe output beam. Similarly, Goldberg and Weller reported a selective angular feedback experiment where they coupled a LDA to a simple external resonator cavity.[24] Their compound cavity functioned as an external mirror laser

oscillator where the LDA provided the oscillator gain. This arrangement produced 410 mW of useful power coupled out of the external cavity in a near-diffraction-limited, single lobe by virtue of angle selective feedback in the cavity to allow only radiation traveling at a specific angle within the LDA to oscillate in the external cavity. MacCormack and Eason achieved an external self-injection-locking configuration and a near-diffraction-limited, single lobe by capitalizing on properties of optical phase conjugation, namely, the need for accurate mirror alignment and exact retroreflection of the array output back into the array elements are automatically satisfied in the phase conjugation process.[25] They observed a single-lobe pattern with 75 percent of the array output power (as high as 450 mW) in a ~2.2 times diffraction-limited beam.

Taking the road less traveled, only a few researchers have explored the approach of combining the two-lobe, far-field intensity pattern into a single lobe. Tatsuno *et al.* showed that anamorphic prism optics are able to create a diffraction limited circular single spot with the aid of a polarization beam combiner or a phase shifter.[26] The anamorphic prism optics worked as beam shapers and spatial filters in the far-field and simultaneously as an astigmatism correction to make a diffraction-limited circular single spot from a fundamental order supermode.

Statement of the Problem

This project will investigate, demonstrate, and evaluate techniques to produce a single-lobe, far-field intensity pattern from a multi-element, phase-locked laser diode array by introducing an optical delay line to one of the two-lobe, far-field intensity patterns before recombining the two lobes into a single lobe in the far field. The scope of the research investigation consists of characterizing a multi-element LDA and demonstrating methods of recombining the far-field lobes into one lobe to maximize the far-field intensity. The experiments will measure relevant operating parameters and far-field intensities. The methods of lobe recombination using an optical delay line will be evaluated.

Approach and Presentation

The fundamental theory of LDs, LDAs, and LDA modes will be presented as the foundation to the investigation. Since the research heavily depends on the spatial and temporal coherence characteristics of the LDA, the definitions and theory of experiments to measure these parameters will be covered.

The experimental investigation will be performed in two phases. The first phase will involve the characterization of the multi-element laser diode array. Specifically, the average output power (including the threshold for lasing), efficiencies, the emission spectra, the beam polarization, and the near- and far-field intensity patterns of the diode

will be observed and measured. From the observations, the far field full width at half maximum (FWHM) of individual lobes and the separation angle between the two lobes will be determined. The spatial and temporal coherence of the output beams will be determined. The experiments will be performed for different currents operating above the lasing threshold current. The second phase will investigate the methods and techniques of forming a single-lobe, far-field beam using an optical delay line and a $\lambda/2$-wave plate. First, the two lobes in the far-field will be combined without an optical delay or $\lambda/2$-wave plate to observe the results of interference upon recombination. Then, the two lobes in the far-field will be combined using glass cubes as an optical delay line and a $\lambda/2$-wave plate to observe the results upon recombination. The far-field intensities of the separate lobes and the combined lobes will be measured for different configurations and at various positions.

II. Theory

Laser Diodes, Laser Diode Arrays, and Laser Diode Array Modes

This section will present the fundamental theories of LDs, LDAs, and LDA modes as the foundation to this investigation. Also, since the research heavily depends on the spatial and temporal coherence characteristics of the LDA, the definitions and theory of experiments to measure these parameters is provided.

Laser Diodes

Several groups succeeded, in 1962, in obtaining laser action by means of carrier injection in a gallium arsenide (GaAs) p - n junction and gave birth to a family of lasers known as semiconductor laser diodes.[27] Today these devices are available from the visible (0.49 μm) to the IR (over 30 μm).[28] The semiconductor laser diode is similar to the light-emitting diode (LED). In fact, they are typically made of the same materials, such as GaAs or gallium aluminum arsenide (GaAlAs), although arranged differently (See Figure 2.). Below a certain threshold current, the LD acts as an LED with spontaneous emission and a broad band, incoherent light output.[29] Above the threshold current, the LD will produce narrow band, coherent light.

When a forward injection current is passed through the LD, as shown in Figure 1, the holes and electrons move into the active region, the p - n junction. Some recombine and give off photons of light. In the LED, the photons can escape as emitted light, or they can be reabsorbed by the p or n material. When a photon is reabsorbed, either a free electron-hole pair is created or heat is generated. On the other hand, in the LD the light is trapped in the active region by the mirror-like end walls. The photons are reflected back and forth and can cause a free electron to recombine with a hole to produce a new photon. Hence the first photon can stimulate the emission of a second photon and produce gain.

For stimulated emission to occur, a strong bias current supplying many carriers (holes and free electrons) is needed. The current continuously injects carriers into the active region where the trapped photons stimulate the carriers to recombine and create more photons. Some of this light is emitted from the mirror-like end surfaces as narrow band, coherent laser light. Since the individual laser emitting element is typically about 6 μm × 1 μm, the resultant radiation intensity pattern in the far-field has large divergence angles as illustrated in Figure 1. Due to the unequal emitting aperture dimensions, the beam diverges less in the axis parallel to the junction plane than in the normal (perpendicular) axis.

Laser diodes are typically fabricated to operate as gain guided or index guided. The early work with LDs involved gain-guided lasers that have no lateral structure; however, because the optical gain is essentially limited laterally by the finite element width, the laser mode is similarly restricted laterally.[13] In gain-guided lasers the injected

charge under each element lowers the index, thereby causing an antiguiding effect with consequent lateral radiation leakage to both sides of the guided mode.[14] As a result, the optical-mode confinement in the plane parallel to the junction is weak and susceptible to changes in drive current. Although gain-guided lasers are gain guided in the plane of the junction, they are index guided in the perpendicular plane. Index guided means optical confinement structures in the plane perpendicular to the junction is provided by the layers above and below the active region and serve as built-in dielectric waveguides.[13] Gain-guided devices radiate with a near Gaussian distribution in the plane perpendicular to the junction, and a more complex pattern in the plane parallel to the junction. If the element width is narrow, the single-element laser emits a single, astigmatic spatial mode.[10] If the element width is not narrow, a multi-longitudinal mode emission spectrum, usually less than 2 nm, results due to spatial hole burning. The polarization ratio of gain-guided laser diodes is typically greater than 10:1 and the polarization axis is in the plane of the junction.

Index-guided lasers, on the other hand, are index guided in the planes parallel and perpendicular to the junction. These lasers, with typical dimensions of 1-2 μm by 3-7 μm, primarily operate at a single longitudinal and transverse mode and provide well-defined and drive-condition independent beams.[14] They are highly coherent emitter devices and radiate with nearly diffraction-limited, minor astigmatic beams. The polarization ratio of index-guided laser diodes is typically above 50:1 and the polarization axis is again in the plane of the junction.

For gain- and index-guided laser diodes, the output power increases almost linearly with injection current once threshold is reached, but, as stated earlier, their maximum power is limited. However, the small size of the elements makes fabricating monolithic arrays of laser diodes with over a thousand laser elements on a single chip possible, drastically increasing the total output power.[11]

One-dimensional (Monolithic) Laser Diode Arrays

The individual elements in a monolithic LDA exhibit characteristics similar to a single-element, gain-guided LD laser. However, when the elements are placed in close proximity to other elements on the semiconductor chip, their electromagnetic fields may influence other elements and cause the individual elements to couple. The coupling of a pair of lasers was first studied experimentally by Ripper and Paoli in 1970 and theoretically by Spencer and Lamb in 1972.[30, 31] The first operational multi-element laser diode (five elements) was reported in 1978 at the Xerox Palo Alto Research Center.[32] Since that time, many different gain-guided, multi-element arrays have been made and studied using GaAlAs or GaAs, emitting in the $\lambda = 0.73\text{-}0.88$ μm range.[14] The output beam from a multi-element array consists of an incoherent sum of beams from each element of the diode, but in some instances, as in a phase-locked array, the output is the coherent sum of the beams.

Laser Diode Array Modes

In the monolithic, phase-locked array, each element defines laterally a fundamental mode where the individual modes are assumed to have different peak-field amplitudes across the array. As mentioned in the introduction, the electric fields from adjacent elements couple when they overlap and provide coherent excitation of each element of the array. Strong coupling occurs if the array elements have the same resonant frequency. Two coupling schemes are of interest: the in-phase mode (0 degree phase difference between adjacent elements) and the out-of-phase mode (180 degree or π phase difference between adjacent elements). These two mode-coupling schemes will be analyzed by a coupled mode theory, assuming an array of N coupled, identical elements, and then from a simple scalar diffraction theory perspective, assuming a uniformly illuminated grating with equally spaced slits corresponding to individual laser elements.

Paoli *et al.*, Epler *et al.*, and Temkin *et al.* have confirmed the coupled-mode analysis best describes the behavior of phase-locked arrays.[33-35] Butler *et al.* published the first coupled mode analysis for an array of N coupled, identical elements.[36,37] They found if coupling occurs only between nearest neighbor elements, an array of N equally spaced elements has N distinct normal modes (or eigenmodes) called array or super modes. Assuming a Gaussian distribution pattern for each laser element, i.e., a single mode, the near-field amplitude (super mode) for the vth array mode can be written as:

$$E_v(x) = E_v(0) \cdot \sum_{m=1}^{N} \sin\left(\frac{m\pi v}{N+1}\right) \cdot \exp\left[-\frac{(x-nD)^2}{2\sigma^2}\right], \qquad (2\text{-}1)$$

where $E_v(0)$ is the electric field at the center of the LDA, x is the lateral displacement

from the center of the array along the junction axis, $v = 1, ..., N$, is the vth array mode,

$m = 1, ..., N$, is the individual array element, $2D$ is the lateral distance between elements,

σ is the Gaussian width, and $n = 2m - (N+1)$ is the Gaussian field displacement for

different elements.[38] From a practical point of view, for many applications, it is desirable

to have the maximum output power in a single-lobe, diffraction-limited far-field pattern

corresponding to $v = 1$ in Equation (2-1).[13] However, even lasers operating in a single-

lobe pattern have beam widths wider than the diffraction-limited beam because arrays can

operate in several array modes simultaneously; i.e., $v = 1$ plus $v = 2$. This gives normal

beam widths two to three times beyond the diffraction limit (FWHM) calculated from:

$$\text{Diffraction Limit} = \frac{\lambda}{NS}, \qquad (2\text{-}2)$$

where λ is the wavelength, N is the number elements, and S is the center-to-center

spacing between elements. Unfortunately, LDAs prefer to operate in the out-of-phase

mode (the mode with the highest gain-to-loss ratio) corresponding to the $v = N$ super

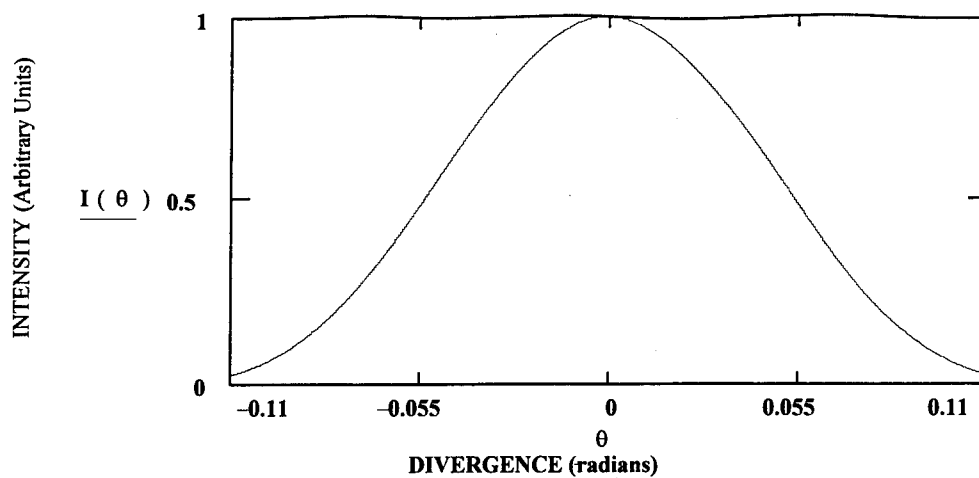mode, resulting in a two-lobe, far-field intensity pattern.

Although coupled-mode analysis best describes the behavior of phase-locked

arrays, Scifres *et al*. first used simple scalar diffraction theory to analyze many

experimental results obtained from single-element lasers and phase-locked arrays.[39] For a single-element laser, a cosine function multiplied by a rectangular function:

$$E_{NF(Single)}(x) = E_{NF}(0) \cdot \cos\left([2\pi]\frac{x}{2b}\right) \cdot rect\left(\frac{x}{b}\right), \qquad (2\text{-}3)$$
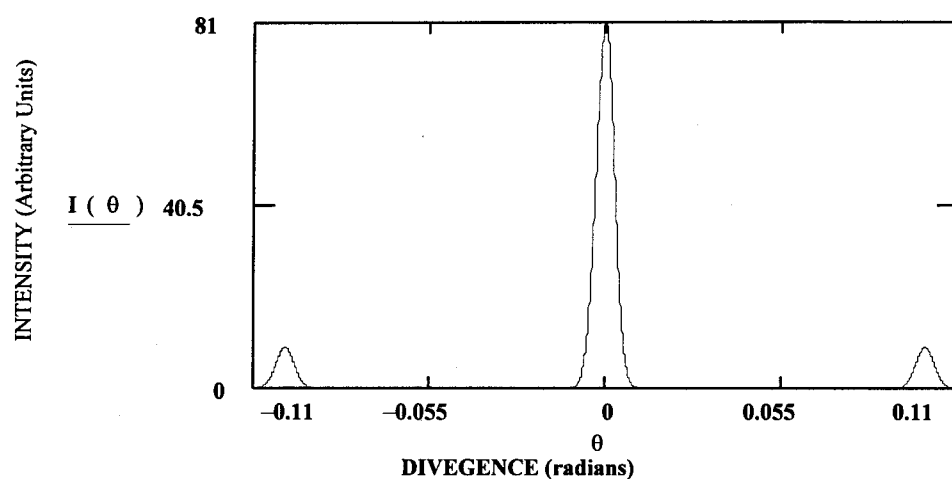
where $E_{NF}(0)$ is the electric field at the center of the LDA, x is the lateral displacement from the center of the element along the junction axis, and b is the array period, approximates the near-field wave front. To find the far-field intensity pattern, scalar diffraction theory predicts the far field (Fraunhofer region) distribution is the Fourier transform of the near-field distribution.[40] The far-field intensity pattern is simply the modulus squared of the far-field, electric-field distribution. Thus, the Fourier transform of the single element near-field electric field distribution, given in Equation (2-3), has a far-field intensity pattern with a single lobe as seen in Figure 3(a) for $b = 10$ μm (See Appendix A for the derivation.). Figure 3(a) shows the maximum peak intensity for the single-element laser is about 1 $|E_{FF}(0)|^2$ (units of intensity), where $|E_{FF}(0)|^2 = I_{FF}(0)$ is the intensity at the center of the far-field pattern. If N lasers were placed together such that no coupling occurred between adjacent elements, the resulting LDA would operate incoherently and the peak intensity, using the example above for a single-element laser, would be N [1 $|E_{FF}(0)|^2$] (units of intensity). For instance, if N = 10, the incoherent LDA would have a peak intensity of about $10 \cdot |E_{FF}(0)|^2$ (units of intensity).

Another possible configuration of the LDA is when the adjacent elements couple 180 degrees out of phase, called a 180 degree phase shift operation, due to a π phase shift

Figure 3. Expected far-field intensity pattern for a single element laser (a) and a rectified, in-phase (b) and out-of-phase (c) LDA.
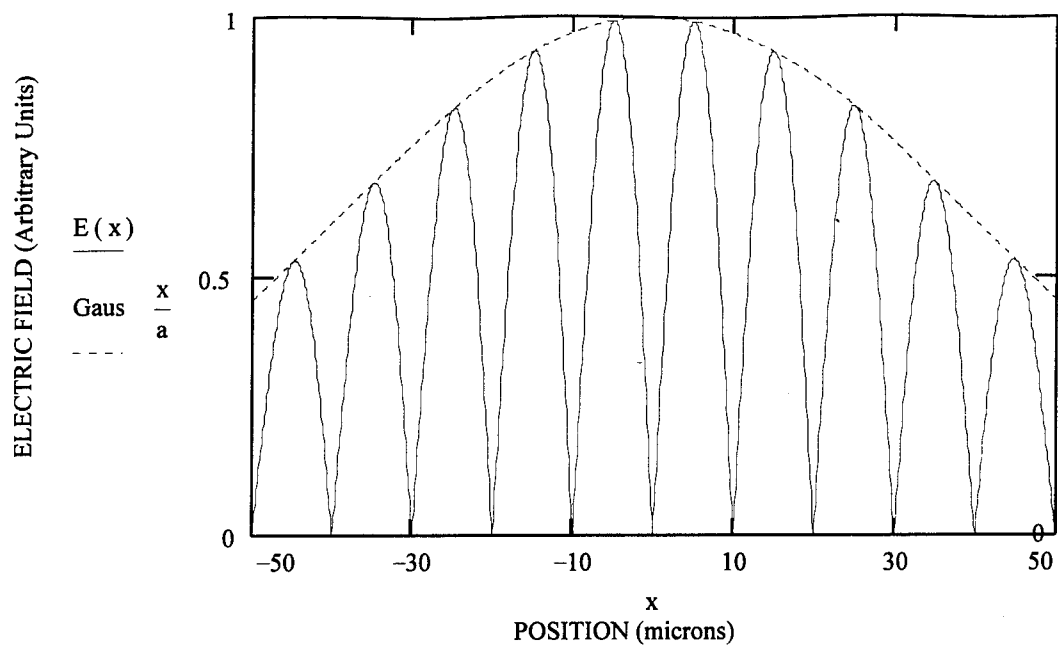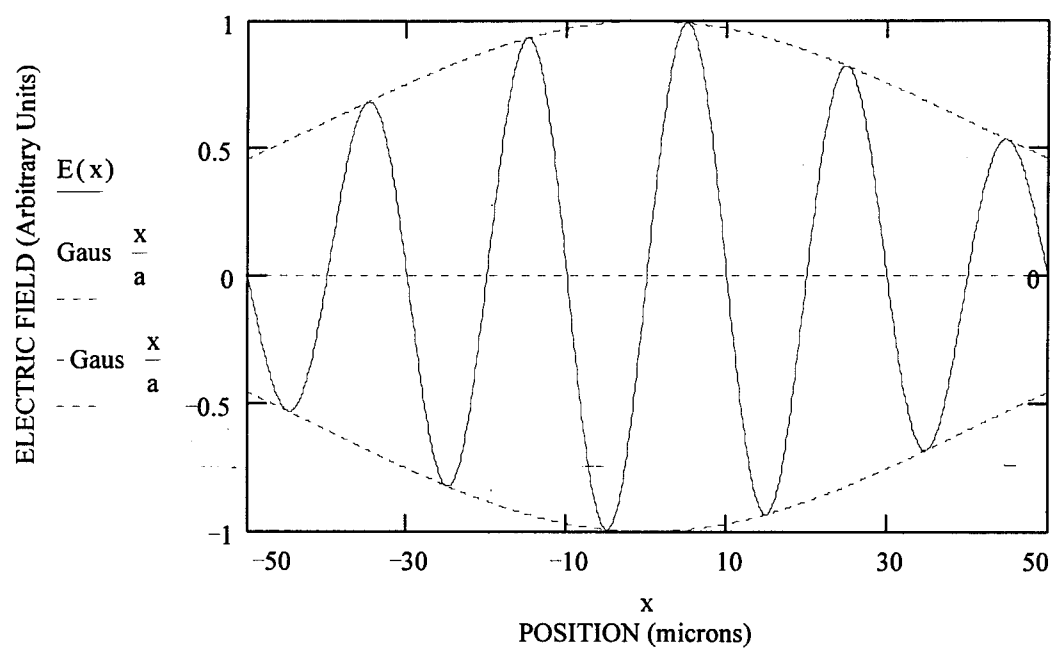
NEAR-FIELD PATTERN (In-phase)

(a)

NEAR-FIELD PATTERN (Out-of-phase))

(b)

Figure 4. Near-field electric-field of a ten-element LDA when it is rectified, in-phase (a) and out-of-phase (b).

between adjacent elements. In this case, the fields between elements destructively interfere and produce nulls in the near-field intensity profile. For an LDA with an even number of elements operating in the out-of-phase mode, a sine function multiplied by a Gaussian function , given below, approximates the combined out-of-phase near-field wave front:

$$E_{NF(Out-of-phase)}(x) = E_{NF}(0) \cdot \sin\left([2\pi]\frac{x}{2b}\right) \cdot \exp\left[-\pi\left(\frac{x}{a}\right)^2\right], \qquad (2\text{-}4)$$

where a is determined from the actual near-field intensity profile. Figure 4(b) shows the approximate array out-of-phase, near-field electric field distribution pattern for $b = 10$ μm and $a = 100$ μm. To find the far-field intensity pattern, the field distribution is again the Fourier transform of the near-field distribution. The far-field intensity pattern is then simply the modulus squared of the far-field, electric-field distribution. Thus, the Fourier transform of the out-of-phase, near-field electric-field distribution, given in Equation (2-4) and Figure 4(b), has a far-field intensity pattern with two displaced Gaussian functions as seen in Figure 3(c) (See Appendix B for the derivation.). Figure 3(c) shows the maximum peak intensity for the out-of-phase mode is 50 $|E_{FF}(0)|^2$ (units of intensity) for each lobe.

When Scifres *et al.* started studying coupled LDAs, they first considered the coupling configuration when all the elements are in-phase, called a 0 degree phase shift operation, since there is no phase difference between adjacent elements. For this case, the

optical fields sum in phase in the space between the elements and the near-field intensity profile is non-zero across the array. For an LDA with an even number of elements operating in-phase, a full-rectified sine function multiplied by a Gaussian function:

$$E_{NF(In-phase)}(x) = E_{NF}(0) \cdot \left| \sin\left([2\pi] \frac{x}{2b} \right) \right| \cdot \exp\left[-\pi \left(\frac{x}{a} \right)^2 \right], \qquad (2\text{-}5)$$

approximates the rectified, in-phase, near-field wave front. Figure 4(a) shows the approximate in-phase, near-field electric-field distribution using Equation (2-5) with $b = 10$ μm (the same as in the previous cases) and $a = 100$ μm. Similar to the far field calculation for an out-of-phase, near-field electric-field distribution, the Fourier transform of the in-phase, near-field electric-field distribution, given in Equation (2-5) and Figure 4(b), has a far-field intensity pattern with a main central lobe and several secondary lobes as seen in Figure 3(b) (See Appendix A for the derivation.). Figure 3(b) shows the maximum peak intensity for the rectified, in-phase mode is 81 $|E_{FF}(0)|^2$ (units of intensity), where $|E_{FF}(0)|^2 = I_{FF}(0)$ is the intensity at the center of the far-field pattern, for the central lobe. This peak intensity is over eight times the intensity for the incoherent, ten-element LDA and about 62 percent higher than the previous out-of-phase mode case using the same parameters.

Is it possible to obtain a maximum power (peak intensity) above the value theoretically achievable with a rectified, in-phase LDA? The answer is yes. If the two far field lobes in Figure 3(c) were combined incoherently (i.e., with no interference) in

21

the far field so their individual peak intensities added, the peak intensity of the resultant single lobe would be a superposition of the individual lobe peak intensities. For example, for the same parameters used to determine the peak intensities for the out-of-phase and rectified, in-phase LDA case above, the addition of the peak intensities of individual lobes for the out-of-phase case in Figure 3(c) would give a combined, single-lobe intensity of $100 \ |E_{FF}(0)|^2$ (units of intensity). The incoherent combination of the two lobes into a single lobe would result in a peak intensity increase of 100 and 23 percent above the maximum theoretical values obtainable using the out-of-phase and rectified, in-phase LDAs, respectively.

Coherence

One solution to increase the output power of an LDA operating in the out-of-phase mode is to incoherently combine the two-lobe, far-field intensity patterns into a single-lobe intensity pattern. But what is coherence and how does it effect the maximum possible intensity upon recombination? Coherence is defined as the property of waves to maintain a definite phase relationship in space and time.[41] For example, two light sources are considered mutually coherent if there exists a fixed phase relationship between them and mutually incoherent otherwise. The coherence of a source can be divided into two classifications: the spatial coherence, relating to the finite extent of a source in space, and temporal coherence, relating to the finite bandwidth, or frequency spread, of the source.

Spatial

Spatial coherence is associated with the finite spatial extent of light sources. A wave is said to exhibit perfect spatial coherence, or lateral coherence, if the phase difference between two fixed points on a plane normal to the direction of propagation is time independent. For example, a laser oscillating in its fundamental transverse-electromagnetic (TEM_{00}) mode is usually spatially coherent over the output beam size, while the sun is spatially coherent over a region of diameter about 0.01 mm.[42] In a laser beam the spatially distributed radiators in the laser are forced to emit radiation in phase and hence a region of coherence exists. If a resonator configuration supports only the TEM_{00} mode of the laser, the spatial distribution of the output is Gaussian and the wave front is of one phase. Since the phase is almost constant over the entire beam, the region of spatial coherence approximately equals the beam size. The spatial coherence of the beam is maintained even after the beam is expanded. Naturally, the spatial coherence of the laser is poor when the laser oscillates in multi-transverse modes. One might ask, "How can someone measure the spatial coherence of a source?" The answer is in the next section.

Young's Double-Slit Experiment

The Young's double-slit experiment is one method used to study spatial coherence by measuring the fringe visibility as a function of slit separation in the

interference pattern produced when light passes through double-slit patterns of varying slit separations. To see how Young's experiment can be used to measure spatial coherence, first consider the basic principles behind the phenomenon of interference and fringe contrast (or visibility).

If two beams of light cross each other without influencing each other, their respective amplitudes, directions of propagation, etc., remain unchanged. However, if the beams are coherent with respect to each other, in the regions they overlap, large variations in intensity are observed. This illustrates the phenomenon of the interference of light. If in the region of overlap, the intensity at a point is either zero or a minimum, this is called total destructive interference. On the contrary, if the intensity is a maximum at a point, it is called total constructive interference. The phenomenon of interference is observed provided the light is both spatially and temporally coherent, a requirement inherent in most laser systems to some degree.

To observe a stable interference (or fringe) pattern, the two interfering waves should have a fixed phase relationship. The interfering waves are therefore derived from the same source wave. Lets consider the complex amplitudes, $\vec{A}_1$ and $\vec{A}_2$, of two waves at any point on a plane given by:

$$\vec{A}_1 = \vec{A}_{10} \cdot \exp\left[i\left(\omega t - \vec{k}_1 \cdot \vec{r}\right)\right] \text{ and } \vec{A}_2 = \vec{A}_{20} \cdot \exp\left[i\left(\omega t - \vec{k}_2 \cdot \vec{r} + \phi\right)\right] , \quad (2\text{-}6)$$

where ϕ is the phase difference between them. When the two waves are superposed, the total amplitude $\vec{A}$ at any point is the sum of $\vec{A}_1$ and $\vec{A}_2$:

$$\vec{A} = \vec{A}_1 + \vec{A}_2 . \qquad (2-7)$$

Since all known optical detectors, for example the eye, respond and detect the modulus squared of the amplitude, called the intensity (I), its value is given by:

$$I = \vec{A} \cdot \vec{A}^* = I_1 + I_2 + 2\left(\hat{e}_1 \cdot \hat{e}_2^*\right)\sqrt{I_1 \cdot I_2} \, \cos(\delta)$$
$$\delta \equiv \left[\left(\vec{k}_1 - \vec{k}_2\right)\cdot r - \phi\right] \qquad , \qquad (2-8)$$

where I_1 and I_2 are the intensities of the individual waves, $\vec{A}^*$ is the complex conjugate of the total amplitude, and $\hat{e}_1$ and $\hat{e}_2^*$ are unit polarization vectors.[41] Thus the overlap or superposition region will vary in intensity with the phase difference. The total intensity will be a maximum when:

$$\delta = 2m\pi , \qquad (2-9)$$

and a minimum when:

$$\delta = (2m+1)\pi , \quad for \quad m = 0, \pm 1, \pm 2, \ldots \qquad (2-10)$$

Consequently, when the waves meet in-phase, constructive interference occurs, and when they meet out-of-phase, destructive interference occurs. The spatial variation of the intensity is the interference pattern. When constructive interference occurs, a bright fringe is formed. Correspondingly, when destructive interference occurs, a dark fringe

forms. The fringe corresponding to $m = 0$ (the zero-order) is always bright. The fringe

contrast, or the visibility (V), of the fringes is defined as:

$$V = \frac{I_{max} - I_{min}}{I_{max} + I_{min}} = \frac{2\sqrt{I_1 I_2}}{I_1 + I_2} |\tilde{\gamma}_{12}(\tau)|, \qquad (2\text{-}11)$$

where I_{max} and I_{min} are the maximum and minimum intensities in the resultant intensity

distribution pattern and $|\tilde{\gamma}_{12}(\tau)|$ is known as the degree of coherence between points one

and two and τ is the time delay between the beams. The degree of coherence between

two waves is defined as:

$$\text{Degree of Coherence:} \begin{cases} |\tilde{\gamma}_{12}(\tau)| = 1 & \text{coherent limit} \\ |\tilde{\gamma}_{12}(\tau)| = 0 & \text{incoherent limit} \\ 0 < |\tilde{\gamma}_{12}(\tau)| < 1 & \text{partial coherence} \end{cases} \qquad (2\text{-}12)$$

The measurement of the spatial coherence therefore involves measuring the fringe pattern

visibility in the interference pattern as a function of slit separation in the Young's double-

slit experiment. Typically, for a given source, the slit separation for which the visibility

falls between $V = 1$ to $V = 0.88$ is taken as the measure of high spatial coherence.[42]


Temporal

The temporal coherence of a source expresses the degree of phase relationship

expected between a wave at a given time (at a fixed position) and the same wave field at a

certain time, τ, later (same position). The temporal coherence arises due to the finite bandwidth of the emission spectral line of a source since all real sources exhibit a spread of wavelengths (frequencies) about an average wavelength. An emission spectral line of finite bandwidth may be considered a combination of many monochromatic, single wavelength, lines which upon superposition reduces the temporal coherence.[41] Due to the finite bandwidth, a wave is limited in space over which a fixed phase relationship is maintained. This length is called the coherence length (l_c).[42]

For example, consider a light source whose emission spectra are given in Figures 5(a) and 5(b) and their visibility curves as a function of optical path length difference are in Figures 5(c) and 5(d).[43] The single Gaussian spectral lineshape in Figure 5(a) with FWHM $\Delta \upsilon = 17.4 \ cm^{-1}$ would give the visibility curve in Figure 5(c). As shown in Figure 5(b), if two separate emission lines with FWHM $\Delta \upsilon = 17.4 \ cm^{-1}$ and one line half the intensity of the other, are separated by $\Delta \upsilon = 30.2 \ cm^{-1}$, the visibility pattern is given in Figure 5(d). The resultant visibility curves in Figures 5(c) and 5(d) show that the sources, whose spectra are given in Figures 5(a) and 5(b), would not interfere if the optical path length difference was longer than about 1 cm and 0.95 cm, respectively.
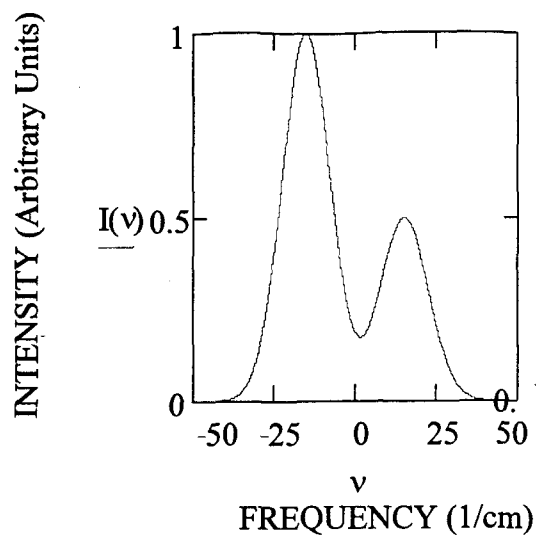
Mathematically, the temporal coherence length of a light source is given by:

$$l_c = c \cdot \Delta t \cong \frac{c}{\Delta \upsilon} = \frac{\left(\overline{\lambda}_0\right)^2}{\Delta \lambda_0}, \qquad (2\text{-}13)$$
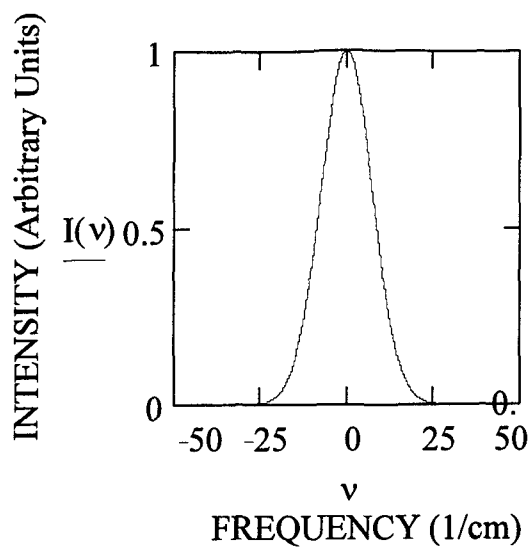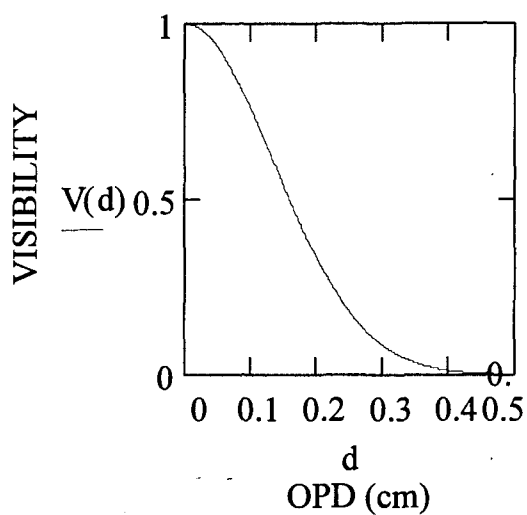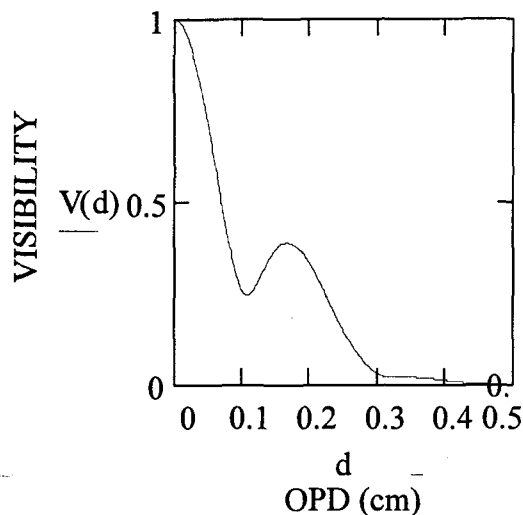
Figure 5. Emission spectrum for a single Gaussian (a) with its visibility curve (c), and a closely spaced, two-peaked Gaussian (b) with its visibility curve (d).

where c is the speed of light in a vacuum, Δt is the coherence time, $\Delta \upsilon$ is the linewidth in [Hz], $\bar{\lambda}_0$ is the mean wavelength, and $\Delta \lambda_0$ is the linewidth in [nm].[43] For example, some lasers have coherence lengths extending up to a few kilometers while white light has a coherence length of around 10^{-4} cm. A wave has perfect temporal coherence and infinite coherence length if the phase difference between two fixed points along the direction of propagation is time independent. To determine the temporal coherence of a source, a Michelson Interferometer is often used to measure the fringe visibility of observed interference patterns as a function of path difference.

Michelson Interferometer

The Michelson interferometer is a versatile instrument of great historic importance capable of demonstrating the formation of interference fringes, establishing zero path differences, measuring the refractive indices of transparent solids, accurately comparing wavelengths, and determining the temporal coherence of a source.

Consider, for example, the Michelson interferometer pictured in Figure 6. The light leaves point S, the source, and falls on the half silvered mirror (or beam-splitter), O. This mirror has a silver coating thick enough to transmit half the incident light and to reflect half. At the beam-splitter the light divides into two waves. One beam proceeds by transmission toward mirror, M1; the other proceeds by reflection toward M2. The waves are reflected at the mirrors and are sent back along their directions of incidence, each
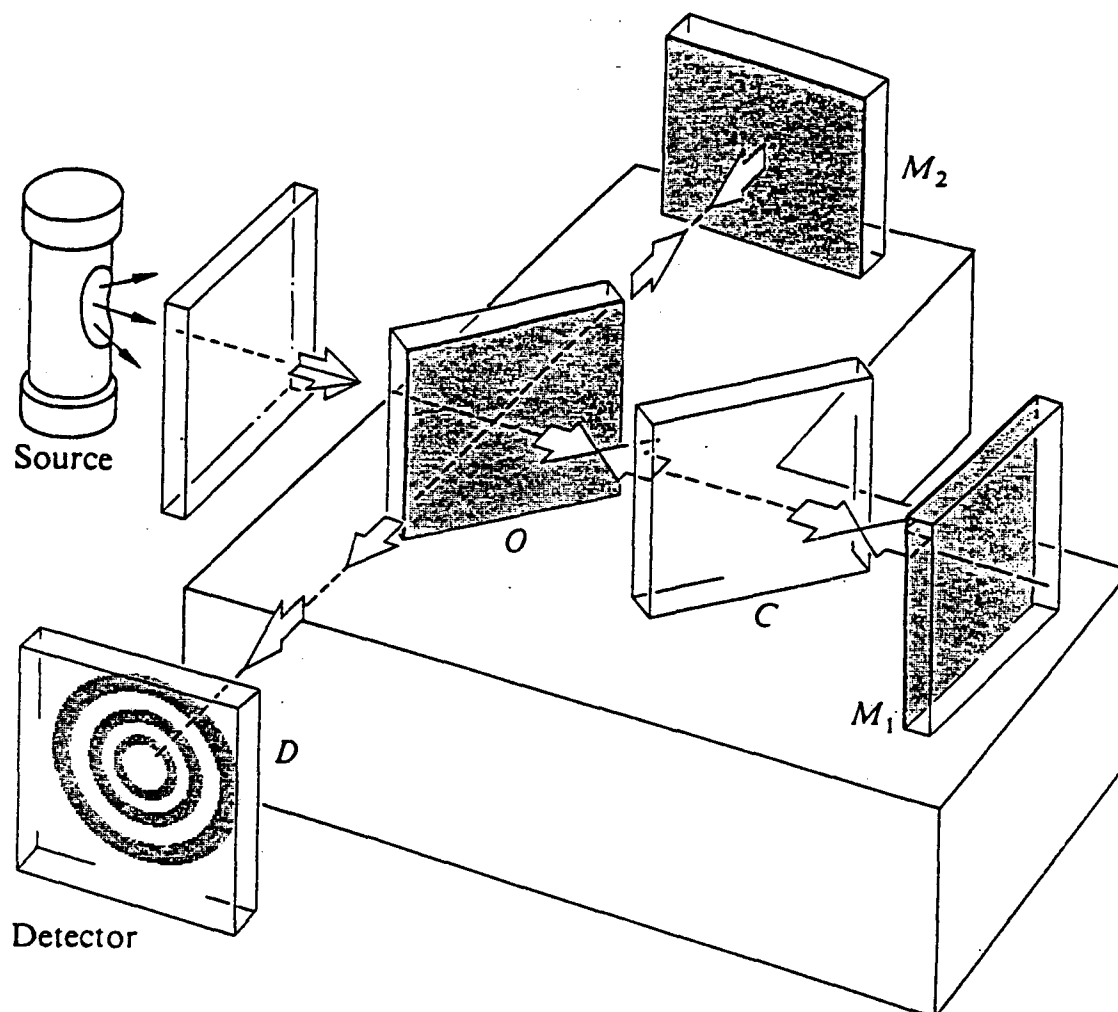
Figure 6. Typical Michelson interferometer configuration. [From Reference 41]

eventually entering the observer's eye or a detector. Since the two waves are coherent, being derived from the same point on the source, they interfere.

If mirrors M1 and M2 are aligned to retroreflect the incident beams, the effect is that of light from an extended source falling on a uniformly thick slab of air, between glass, whose thickness is d. Interference fringes appear caused by small changes in the angle of incidence of the light from different points on the extended source as it strikes an equivalent air film. For thick films, a path difference of one wavelength can be made by a very small change in incident angle.

If M2 is moved backward or forward, the thickness of the equivalent air film is changed. When the mirror, M2, is moved forward or backward, the first bright circular fringe moves into or out of the center of the fringe pattern. For instance, consider the circular and straight fringe patterns shown in Figure 7. If only one fringe moves, the path of the light beam striking M2 moves by one wavelength. This means (since the light passes twice through the equivalent air film) the mirror must have moved one-half of a wavelength.

Notice in Figure 6 that the light rays going to mirror, M2, pass through O three times whereas the other light rays only pass through O once. To ensure each beam of light rays passes through equal thicknesses of glass, a compensator plate, C, is inserted in the O-to-M1 arm of the interferometer. The compensator is an exact duplicate of the beam-splitter with the exception of any thin coatings on the beam-splitter. It is positioned at an angle of 45 degrees so O and C are parallel to each other. With the compensator
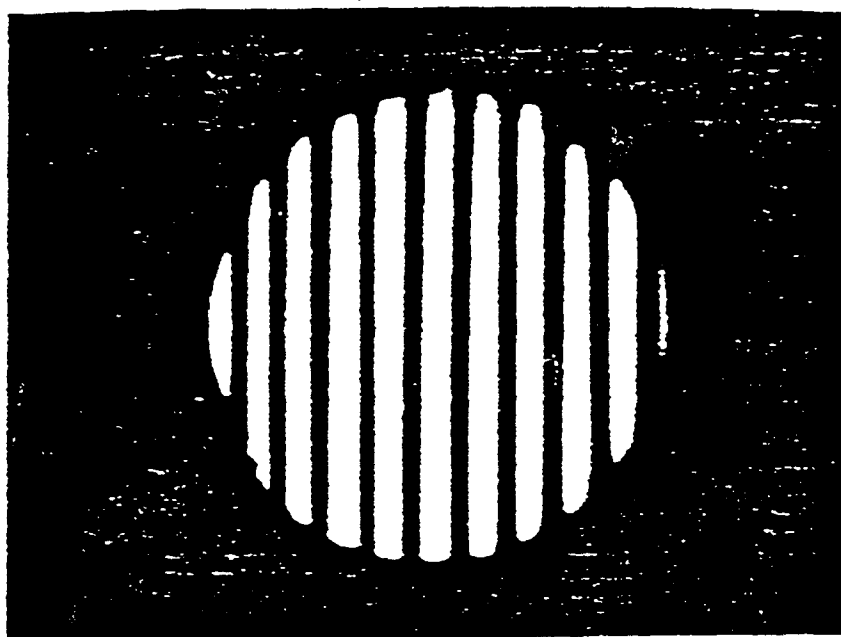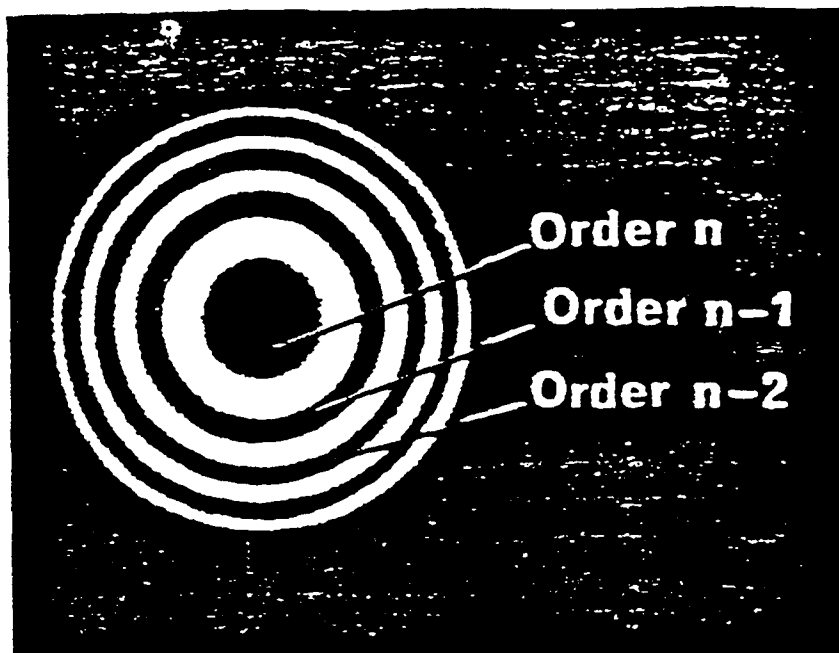
Figure 7. Pattern of circular and straight fringes. [From Reference 44]

plate in place, any optical path difference comes from the actual path difference. Also, due to the dispersion of the beam-splitter, the optical path is a function of λ. For a perfectly monochromatic wave, fringes are seen for any path difference, but when a finite band of wavelengths is present, a sufficiently large path difference will result in a large range of phase differences for the various wavelengths present and so the fringes disappear. An interferometer without the compensator plate can only be used with a quasi-monochromatic source. On the contrary, an interferometer with the compensator plate negates the effect of dispersion so even a source with very broad bandwidth, such as white light, will generate observable fringes.

III. Experiments and Results

Characterization of Laser Diode Array

The laser diode array used for this study is a commercial GaAlAs, monolithic, ten-element, gain-guided, laser (Spectra Diode Laboratories Model SDL 2410-C, Serial Number P413), with 1 μm $\times$ 6 μm $\times$ 250 μm elements on 10 μm centers. This gives an effective one-dimensional aperture of about 1 μm $\times$ 100 μm. The elements of the array are evanescently coupled, operate in multi-longitudinal modes, and generate up to 100 mW CW at room temperature in a two-lobe, far-field intensity pattern. Since this LDA is used for all of the experiments to follow, its average output power (including the threshold current for lasing), efficiencies, the emission spectra, the beam polarization, and the near- and far-field intensity patterns of the diode were observed and measured. From the observations, the FWHM of individual lobes and the separation angle between the two lobes were found. The spatial and temporal coherence of the output beams were determined. The experiments were performed for different currents at room temperature.

Output Power and Current

The CW output power and current of the laser was measured for different currents, as shown in Figure 8, using an IR calibrated Newport digital power meter
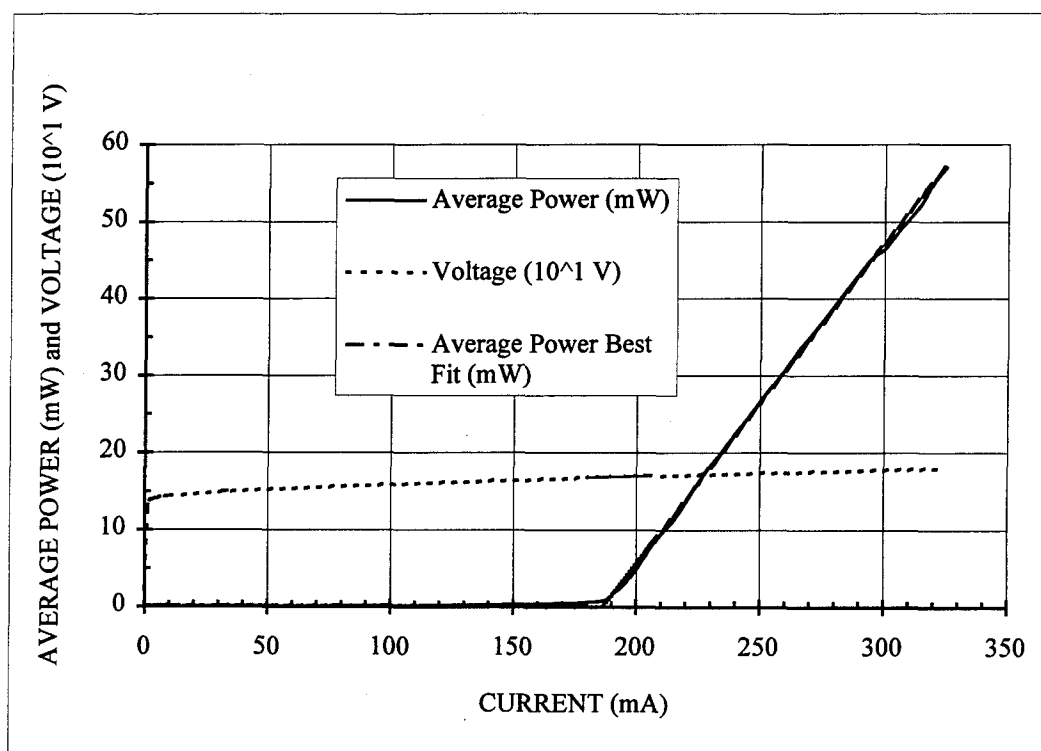
Figure 8. Laser diode array average output power and voltage versus current.

(Model 815 Series) and a multimeter, respectively. From Figure 8 the laser diode array was found to have a linear relationship between the average output power and current for currents above the measured lasing threshold, $I_{th} = 187 \pm 2$ mA, with a differential power efficiency (the slope efficiency), $\eta_{dp} = 0.42 \pm 0.01$ mW/mA. These experimental values for the lasing threshold current and differential power efficiency agree exactly with the manufacturer's theoretical values.[12] The differential quantum efficiency, η, the photons emitted per electron injected, was found to be $\eta = 0.42 \pm 0.01$, the same as the theoretical value.[45]

Emission Spectra

The emission spectra of the LDA were measured using a Jarrel-Ash 0.5 Meter Ebert Scanning Spectrometer (Model 82-020), calibrated with an Oriel xenon calibration pen ray lamp from 800-850 nm, and fit with a least squares routine. This array was found to have emission spectra as shown in Figures 9(a)-9(c) for different currents. The LDA required about 20 minutes after each current adjustment before the emission spectrum stabilized since the laser is sensitive to drive current and temperature effects. In Figure 9(a) the emission spectrum of the LDA at 200 mA (1.07 I_{th}) has two predominant longitudinal mode lasing peaks centered around 829.0 nm and ranging from approximately 828.3-829.6 $\pm$ 0.3 nm, about 1.3 nm wide at the base. At 240 mA
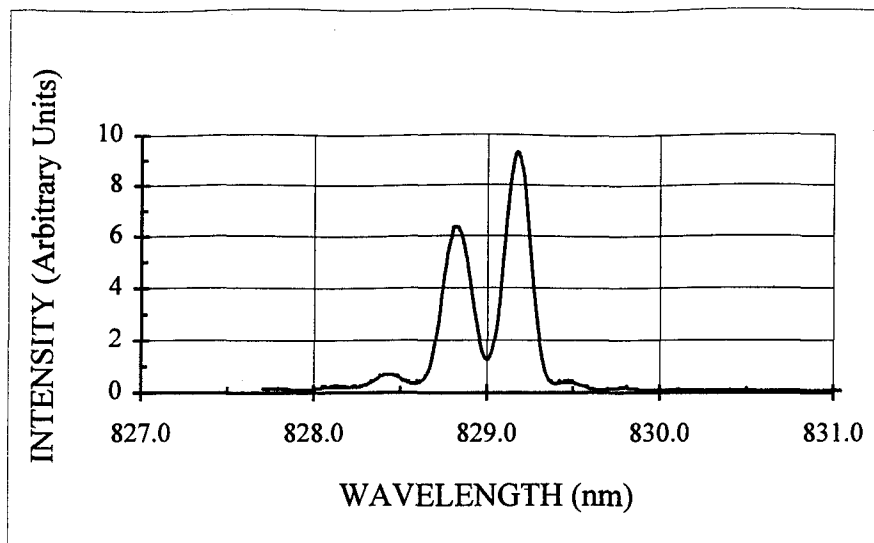
(a)
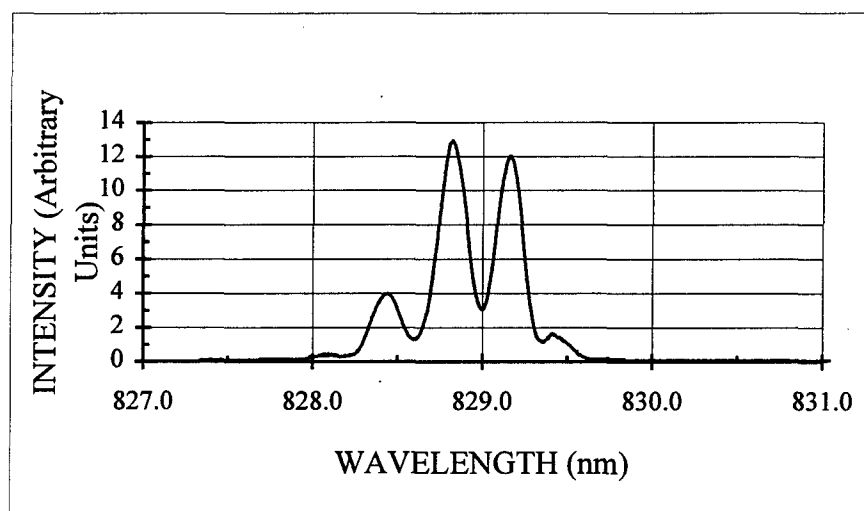
(b)
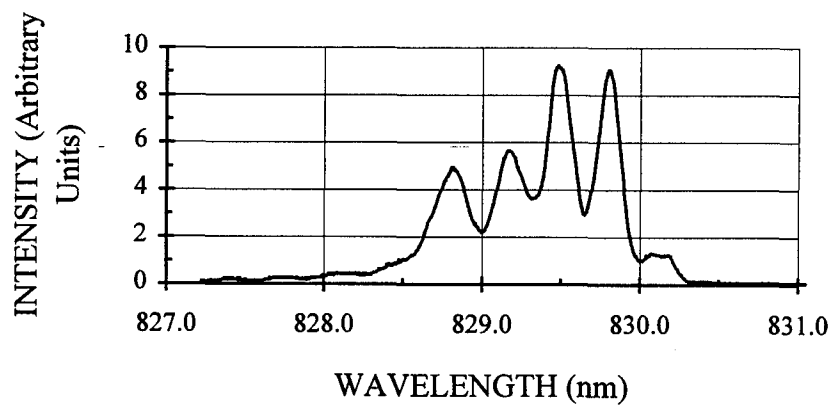
(c)

Figure 9. Emission spectrum of the LDA operating at 200 mA (a), 240 mA (b), and 300 mA (c).

(1.28 I_{th}), a third significant lasing peak appeared, as shown in Figure 9(b), and the emission spectrum widened to about 1.6 nm at the base, ranging from

828.0-829.6 ± 0.3 nm, but still centered around 829.0 nm. Figure 9(c) shows that at 300 mA (1.60 I_{th}) a fourth additional lasing peak added to the previous spectrum ranging from about 828.3-830.3 ± 0.3 nm (2.0 nm wide at the base), wider than the previous spectra, but centered near 829.3 nm. This is probably due to diode heating effects that can cause an upward shift in wavelength of the emission spectrum pattern. The manufacturer quoted the wavelength of the LDA as 830 nm at a test temperature of 25 C, which adjusting for a room temperature of 21.5 C, is equal to 829.1 nm, within experimental error.[12] The periodic structure in each of the figures had spacing between cavity longitudinal modes, $\Delta\lambda$ = 0.33 ± 0.02 nm. The theoretical value is determined from:

$$\Delta\lambda \approx \frac{\lambda^2}{2nL(1.25)},$$ (3-1)

where λ is the wavelength, n (= 3.6) is the effective index of refraction, L is the cavity length, the factor 1.25 is the weighted dispersion of the various array layers, and hence $\Delta\lambda$ = 0.31 ± 0.03 nm, within the ranges of errors. The average FWHM of the longitudinal mode lasing peaks for all the collected emission spectrum data was 0.19 ± 0.01 nm.

Polarization

The laser diode beams were determined with a linear polarizer to be predominately linearly polarized in the plane parallel to the p - n junction. The ratio of output power for the polarizer oriented parallel versus normal to the p - n junction is given in Figure 10(a) and shows an increase in the ratio from 2:1 to 94:1 as the respective output powers increase. Figure 10(b) shows the ratio of linear polarization versus current increases from 2:1 at 170 mA (below the lasing threshold current) to 94:1 at 300 mA, in agreement with the manufacturer's specification values.

Intensity Patterns

All the following intensity patterns and analysis were obtained using General Electric's TN2509 CID array camera to monitor the patterns, Coherent's BEAMCODE 5.25 software to capture, store and analyze the patterns and beam profiles, and Applied Techniques' Pizazz Plus 1.0 software for monitor screen dumps.

Near-field Intensity Pattern

Figure 11 shows the near-field intensity pattern of the array with the array operating at 300 mA. The near-field intensity pattern is observed by placing a camera or
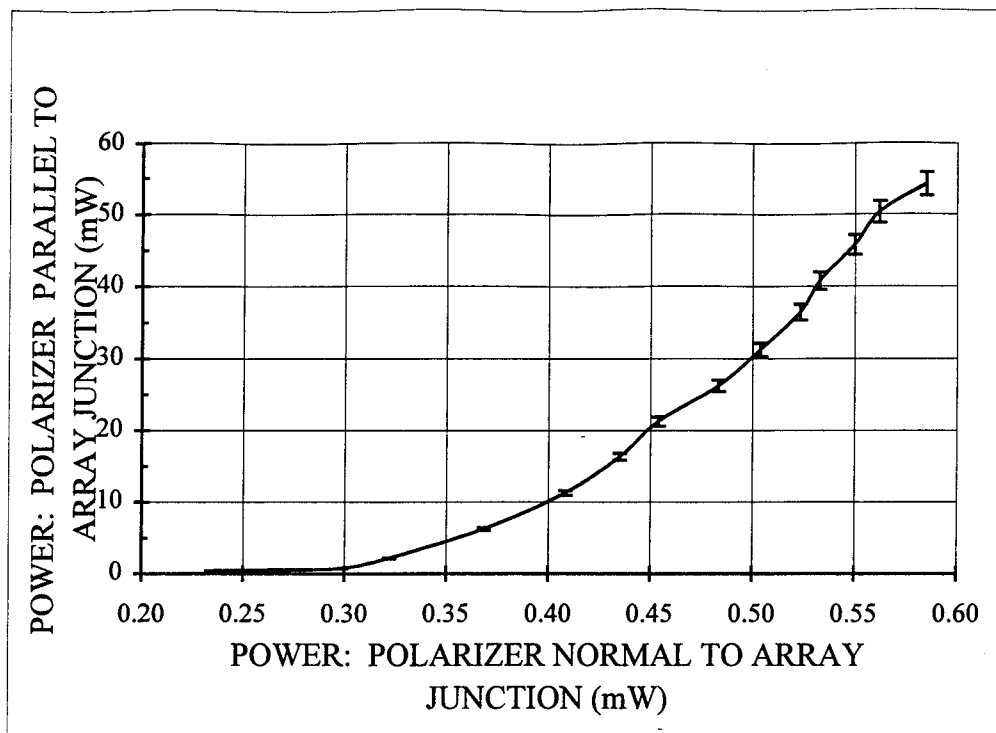
(a)
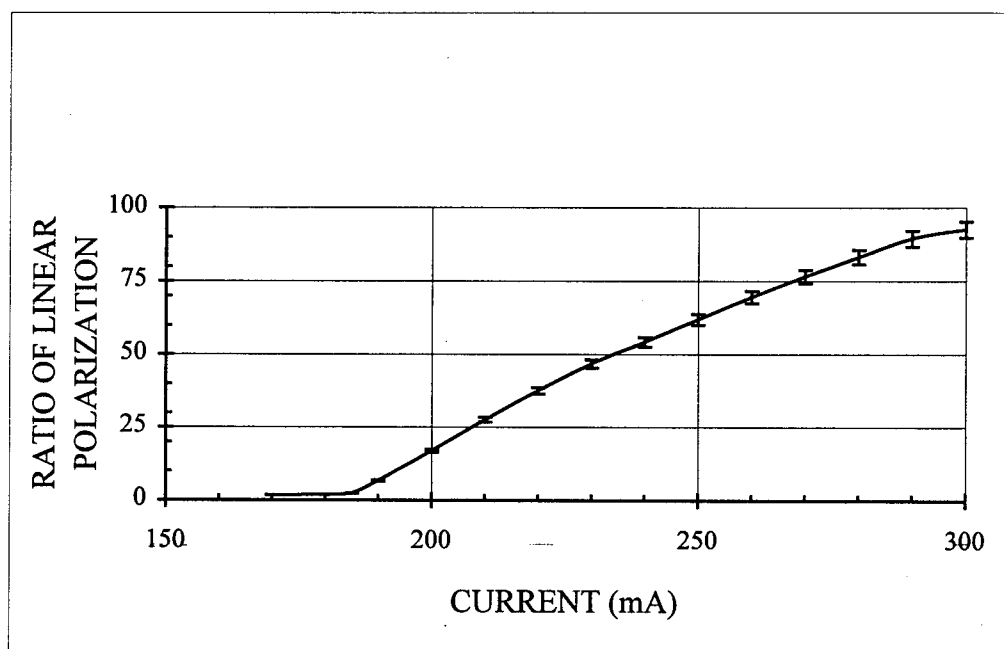
(b)

Figure 10. LDA linear polarization ratio (a) and
linear polarization ratio versus current (b).

COLOR SCALE

253 ->	
225 ->	
210 ->	
195 ->	
180 ->	
165 ->	
150 ->	
135 ->	
120 ->	
105 ->	
90 ->	
75 ->	
60 ->	
45 ->	
30 ->	
15 ->	
0 ->	

(a)

X-AXIS

Y-AXIS
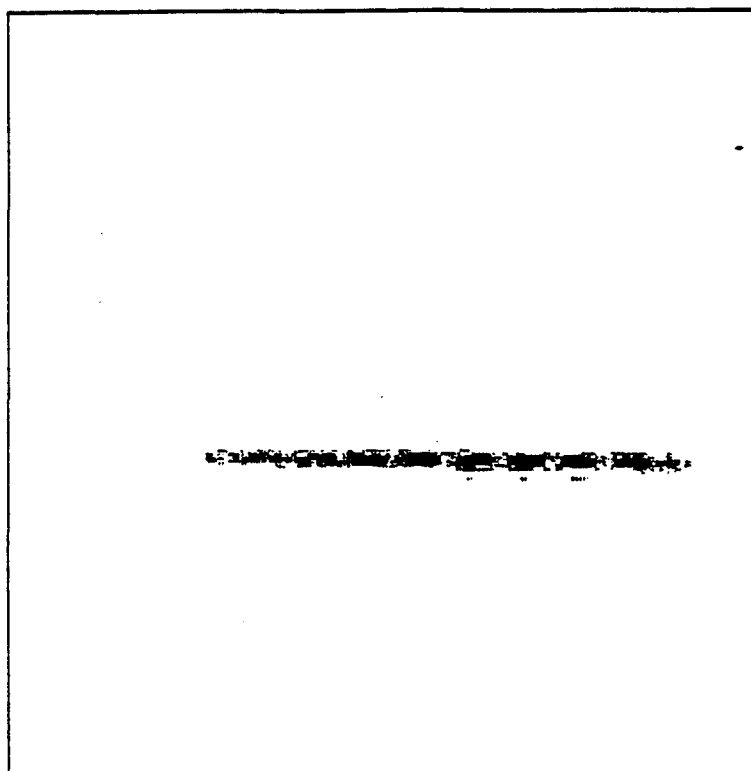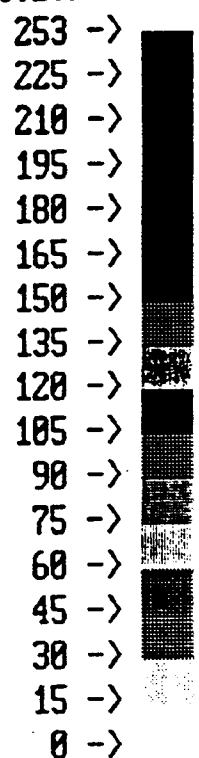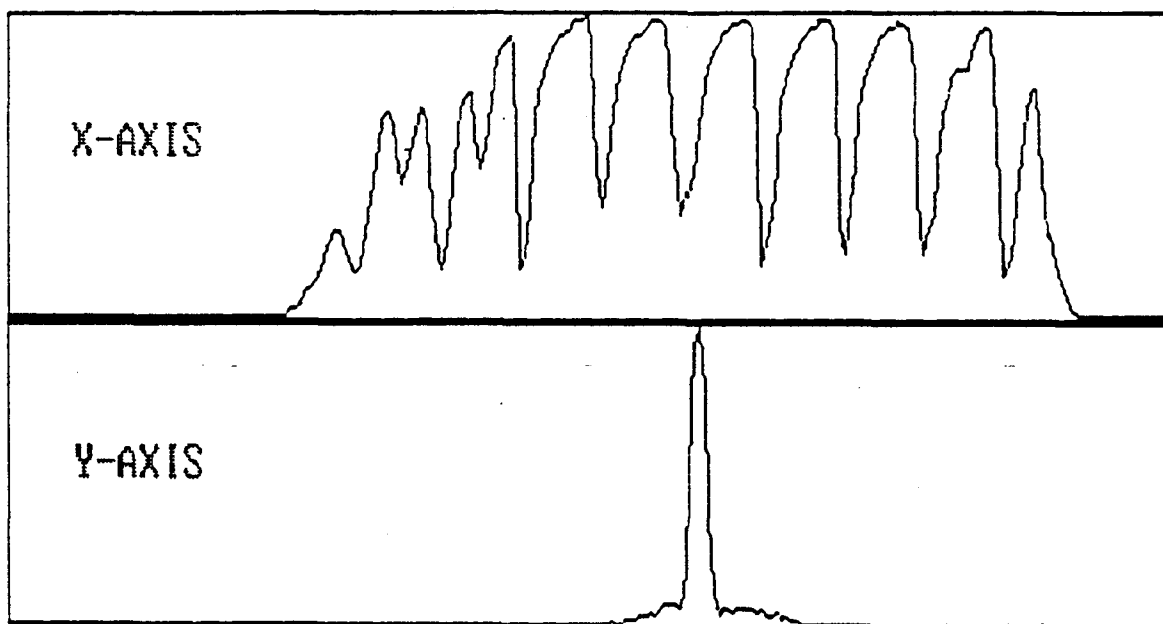
(b)

Figure 11. Near-field intensity pattern of LDA showing the contour plot (a) and profiles (b).

detector in the image plane as described in Appendix C. The contour plot in Figure 11(a) shows a one-dimensional array of ten closely spaced elements of varying intensities. The profile plots in Figure 11(b) clearly show ten Gaussian-like peaks, corresponding to the ten array elements, in the x-axis profile and a single Gaussian-like peak in the y-axis profile. The x-axis profile shows the elements near the center of the array have higher relative intensities than the elements on the ends.

Far-field Intensity Patterns

The far-field intensity pattern of an individual element of the array is seen in Figure 12 with the array operating at a current of 200 mA. The contour plot in Figure 12(a) was obtained by placing a single 80 μm slit in the near-field plane of the array, isolating the fourth element, and then recording the pattern in the far-field plane. The profile plots in Figure 12(b) show a single profile in the x-axis plot and a rectangular-type profile in the y-axis profile. Using the Gaussian fitting routine in BEAMCODE, the FWHM and Gaussian correlation coefficient (if the correlation coefficient is 1.0, it is a perfect Gaussian) for the element in Figure 12 were found to be 2.97 ± 0.03 mm and 0.92, respectively. On average for different currents, the FWHM and Gaussian correlation coefficient for the ten individually imaged elements were 3.0 ± 0.2 mm and 0.92 ± 0.02. The diffraction limit of 7.9 degrees calculated using Equation (2-2)

COLOR SCALE

| 250 -> |
| 225 -> |
| 210 -> |
| 195 -> |
| 180 -> |
| 165 -> |
| 150 -> |
| 135 -> |
| 120 -> |
| 105 -> |
| 90 -> |
| 75 -> |
| 60 -> |
| 45 -> |
| 30 -> |
| 15 -> |
| 0 -> |

(a)

X-AXIS

Y-AXIS
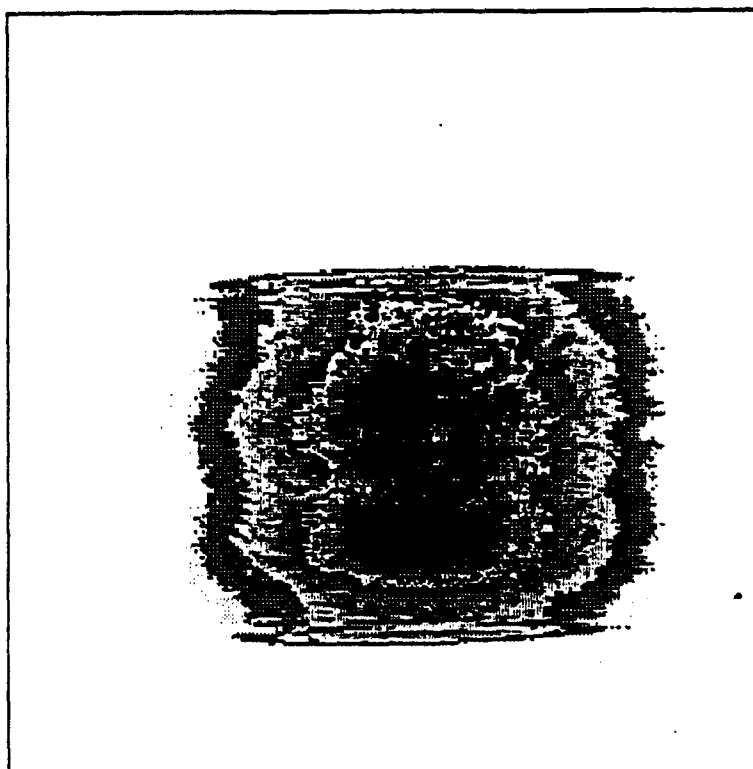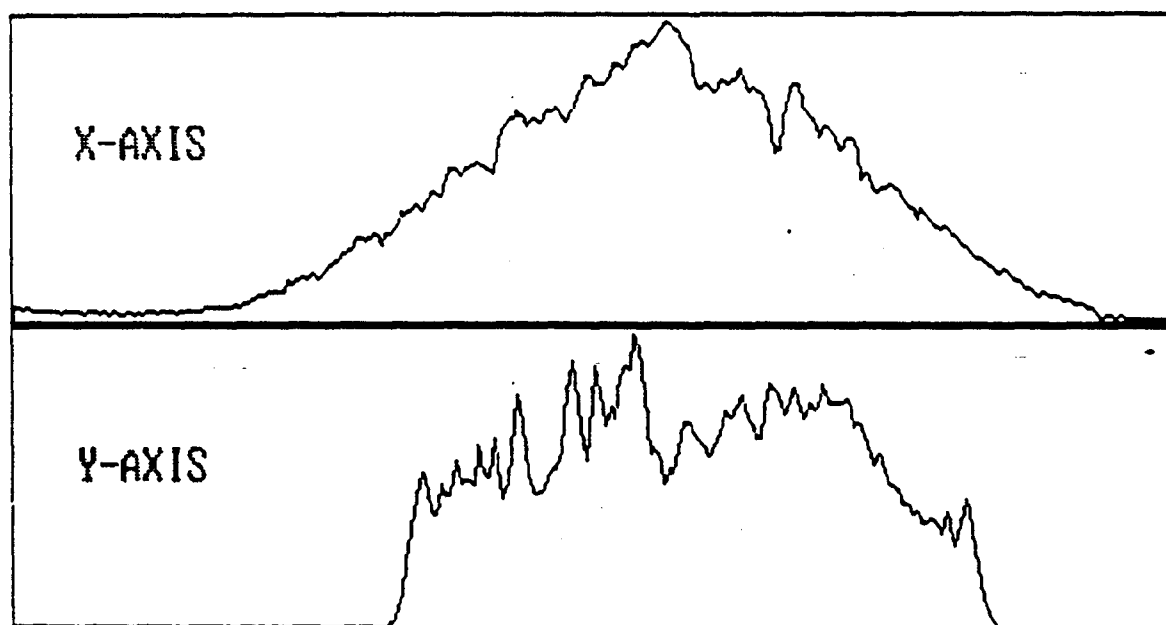
(b)

Figure 12. Far-field intensity pattern of a single element of the LDA showing the contour plot (a) and profiles (b).

compares favorably to the experimental divergence angle determined to be 8.4 ± 0.6 degrees for a 6 μm wide element.

Significantly different than the single-element far-field pattern, the far-field intensity pattern of the LDA is the two lobe pattern characteristic of a π phase difference between the adjacent elements of the array. The far-field intensity pattern is observed by placing a camera or detector in the far-field plane whose location is determined as described in Appendix C. The experimental setup used to observe the far-field intensity patterns is shown in Figure 13 where the LDA is the source; $L1$ is a 20× near-IR, positive microscope objective lens with focal length f_1 = 0.8 cm; $L2$ is a positive lens with f_2 = 15.0 cm; $L3$ is a cylindrical lens with f_3 = 15.0 cm; the mirrors are independently adjustable steering mirrors; $L4$ is a positive lens with f_4 = 16.7 cm; the filter is a neutral density filter; the CID is the General Electric camera; and the frame grabber is the software and hardware required to capture, store, and analyze the images.
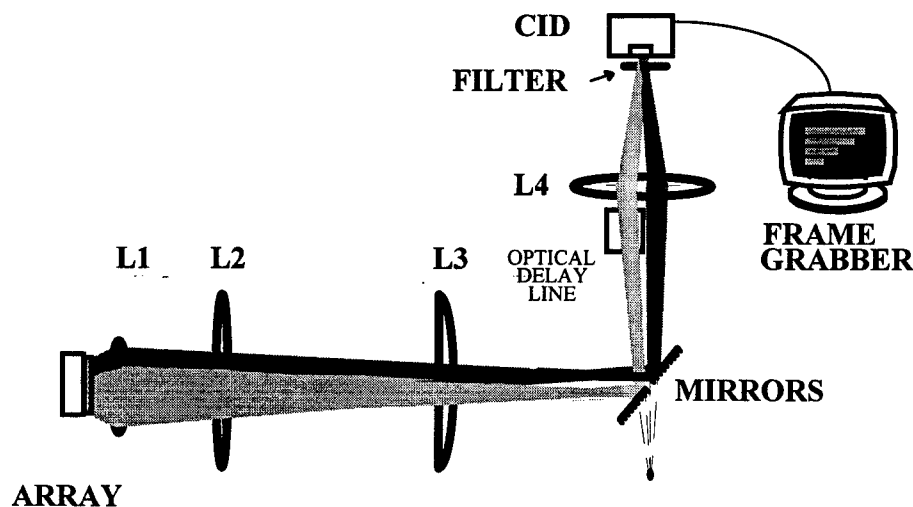
Figure 13. The experimental setup used to view and analyze far-field intensity patterns.

As shown in Figures 14(a)-14(c), the far-field intensity pattern of the LDA is indeed a two-lobe pattern. Figure 14(a) is the far-field intensity pattern imaged in the far-field at a current of 200 mA. The contour plot in Figure 14(a) shows two distinct lobes with highest intensity in the centers of the patterns. The profile plots in Figure 14(a) show an x-axis profile with two Gaussian-like curves and a y-axis profile plot similar to the single-element y-axis profile. The FWHM and Gaussian correlation coefficients of the left and right lobes in Figure 14(a) were found to be 0.61 ± 0.03 mm; 0.92, and 0.64 ± 0.03 mm; 0.92, respectively. The measured beam divergence angles of 1.70 ± 0.09 degrees for the left lobe and 1.79 ± 0.09 degrees for the right lobe is 3.5 and 3.7 times the diffraction limit of 0.48 degrees as determined from Equation (2-2) for a 100 μm aperture. However, this is understandable since due to the simultaneous operation of several array modes, the beams are usually more than two to three times the diffraction limited beamwidth. The separation of the peaks measured 1.88 ± 0.03 mm which gives a far-field divergence angle between lobes of 5.3 ± 0.3 degrees.

Figure 14(b) is the far-field intensity pattern imaged in the far-field with the current at 240 mA. The contour plot in Figure 14(b) shows two lobes, similar to Figure 14(a). The profile plots in Figure 14(b) show an x-axis profile with two Gaussian-like curves and a y-axis profile plot similar to the previous y-axis profiles. The FWHM and Gaussian correlation coefficients of the left and right lobes in Figure 14(b) were found to be 0.84 ± 0.03 mm; 0.91, and 0.84 ± 0.03 mm; 0.92, respectively. The measured beam divergence angles of 2.30 ± 0.09 degrees for the left and right lobes is
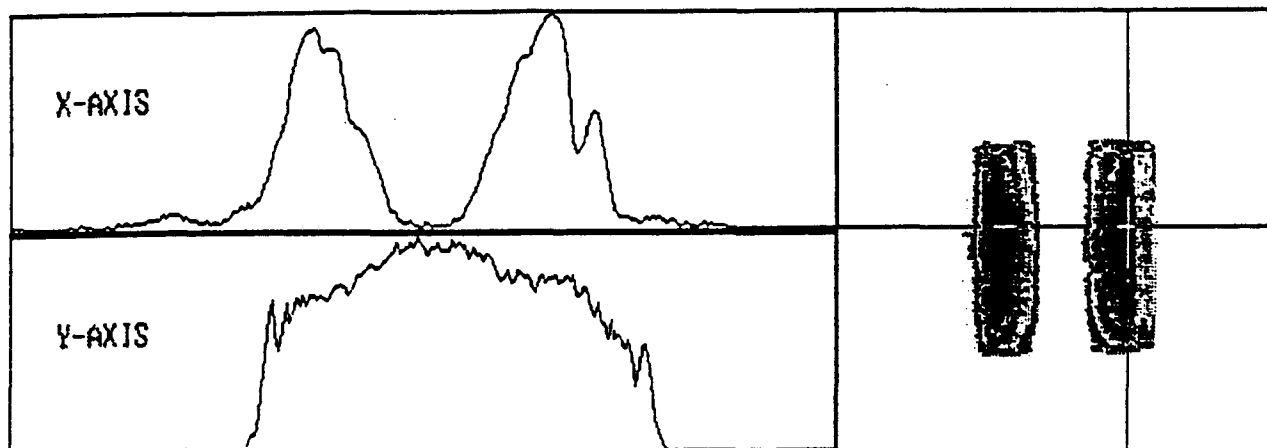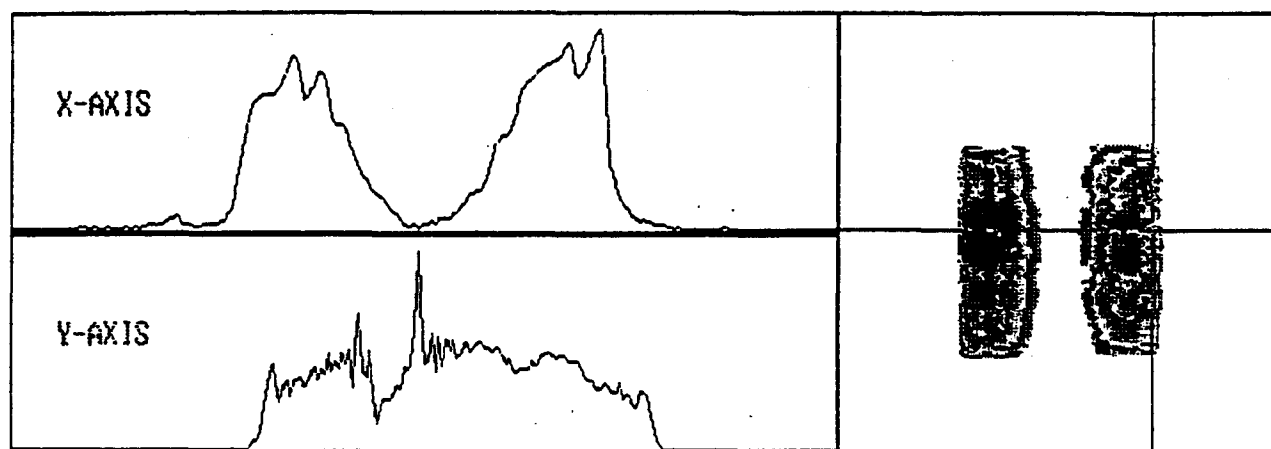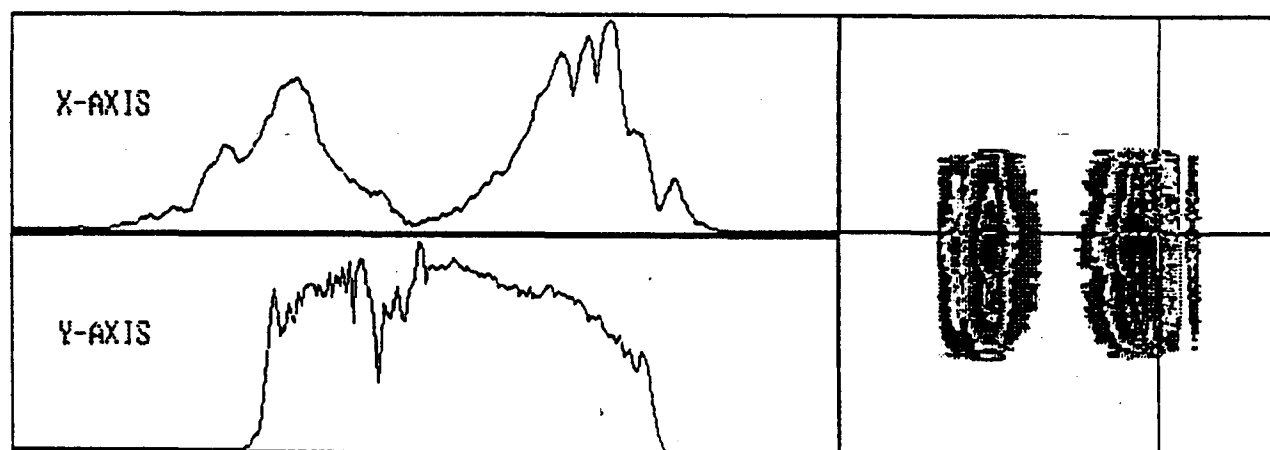
Figure 14. Far-field intensity patterns of the LDA operating at 200 mA (a), 240 mA (b), and 300 mA (c).

4.8 times the diffraction limit of 0.48 degrees as determined for a 100 μm aperture. The increase in the divergence angles is expected as the current increases since more array modes are running simultaneously. The separation between the peaks increased to 2.14 ± 0.03 mm, a 13 percent increase from Figure 13, giving a far-field divergence angle between lobes of 6.0 ± 0.3 degrees.

As in the previous two figures, Figure 14(c) shows the two lobe, far-field intensity pattern, but now the current is at 300 mA. The contour plot in Figure 14(c) is similar to the previous patterns, but a few strong vertical intensity lines appear. The profile plots in Figure 14(c) show an x-axis profile with two Gaussian-like curves; however, the right lobe shows some peaks under the Gaussian envelope as expected from the contour plot image. The y-axis profile plot is similar to the previous y-axis profiles. The FWHM and Gaussian correlation coefficients of the left and right lobes in Figure 14(c) were found to be 1.06 ± 0.03 mm; 0.91, and 1.07 ± 0.03 mm; 0.88, respectively. The experimental divergence angle values of 3.0 ± 0.1 degrees for the left and right lobes is 6.3 times the diffraction limit of 0.48 degrees as determined for a 100 μm aperture. The separation of the peaks again increased to 2.39 ± 0.03 mm, a 27 percent increase from Figure 14(a) and a 11 percent increase from Figure 14(b), which gives a far-field divergence angle between lobes of 6.7 ± 0.3 degrees. This increase in the far-field divergence angle with increasing current is consistent with the excitation of higher-order supermodes.

Coherence Measurements

Spatial

The Young's double-slit experiment was used to study the spatial coherence of the LDA by measuring the fringe visibility as a function of slit separation in the interference pattern produced when the beams passed through double-slit patterns of varying slit widths and spacings. All the measurements in Table 1 were made with the double-slit patterns inserted into the individual beam paths in the far-field plane of the LDA at a current of 240 mA. For slit pattern A, the smallest slit separation, the array exhibited high spatial coherence in the planes parallel and normal to the array junction. As the slit separation, or spacing, increased for slit patterns B through E as shown in Table 1, the spatial coherence for the left and right lobes remained high when the slit patterns were

TABLE 1

SPATIAL COHERENCE FOR DIFFERENT SLIT SPACINGS

Double-Slit Patterns			Slits Normal to Array Junction				Slits Parallel to Array Junction			
			Left Lobe		Right Lobe		Left Lobe		Right Lobe	
Slit Pattern	Width (mm)	Spacing (mm)	Fringe Visibility	Standard Deviation	Fringe Visibility	Standard Deviation	Fringe Visibility	Standard Deviation	Fringe Visibility	Standard Deviation
A	0.04	0.125	0.94	0.01	0.95	0.01	0.99	0.01	0.99	0.01
B	0.04	0.250	0.43	0.01	0.43	0.01	0.98	0.01	0.97	0.01
C	0.08	0.250	0.43	0.01	0.45	0.01	0.97	0.03	0.97	0.03
D	0.04	0.500	0.17	0.01	0.16	0.02	0.97	0.01	0.96	0.01
E	0.08	0.500	0.18	0.01	0.17	0.01	0.98	0.03	0.98	0.03

aligned parallel to the array junction, but decreased rapidly to below V = 0.20 when the patterns were placed in positions normal to the junction of the array.

Temporal

The Michelson interferometer was used to study and estimate the temporal coherence of the LDA by measuring the fringe visibility of interference patterns as a function of path difference. The zero path length difference position of the interferometer was first determined using a white light source. The two-lobe, far-field pattern was then passed through the interferometer and imaged on the CID at zero and increasing path length differences. The alignment mirrors of the Michelson were adjusted so the two lobes could be combined and forced to interfere in the far-field. At zero path length difference, the resulting interference patterns approached V = 0.95 when the lobes interfered in the plane normal to the junction of the array, the high spatial coherence plane. Since the Michelson interferometer was measured to have a 53:47 beam splitter at 829 nm, the fringe visibility was not measured nor is expected to be 1.0 at zero path difference. However, no interference pattern resulted when the lobes were combined and aligned to interfere in the plane parallel to the junction of the array, the low spatial coherence plane. When the near field was imaged on the CID and adjusted to combine and interfere after passing though the interferometer, the same visibility results were found as above for the planes normal and parallel to the junction of the array. The results

obtained when the lobes and elements were combined for interference in the plane parallel to the junction of the array are surprising. One would expect a temporally coherent source would interfere in any axis when combined; however, this was not observed for the low spatial coherence axis. The reason may be rooted in the low spatial coherence measured in that plane or in the out-of-phase, near-field electric field.

To estimate the temporal coherence and coherence length of the lobes of the LDA, Figure 15 shows the visibility versus path length difference for the LDA operating at a current of 240 mA with the two lobes combined and interfered with each other. The graph in Figure 15(a) shows the visibility decreases as the path length difference increases to 0.35 mm, then the visibility begins to increase. The linear best fit is plotted as a comparison to the visibility curve, but is not expected to be linear. The linear plot crosses the path length difference axis at 0.47 ± 0.03 mm, which corresponds to an estimated coherence length of about 0.94 ± 0.06 mm in agreement with the manufacturer's quoted estimate of about 1 mm. However, this curve corresponds to the first peak and trough in Figure 5(d) since the visibility in Figure 15(a) has begun to increase for optical path length differences past 0.35 mm. This is expected since the emission spectrum of the LDA at 240 mA, as shown in Figure 9(b), shows at least four (possibly more) closely spaced peaks of varying intensities which would produce a more complicated visibility curve than idealized in Figure 5(d) for a two-peaked spectrum.

On the other hand, Figure 15(b) shows the visibility versus path length difference curve plotted for the LDA, operating at 240 mA, at the peaks of the visibility curve, a
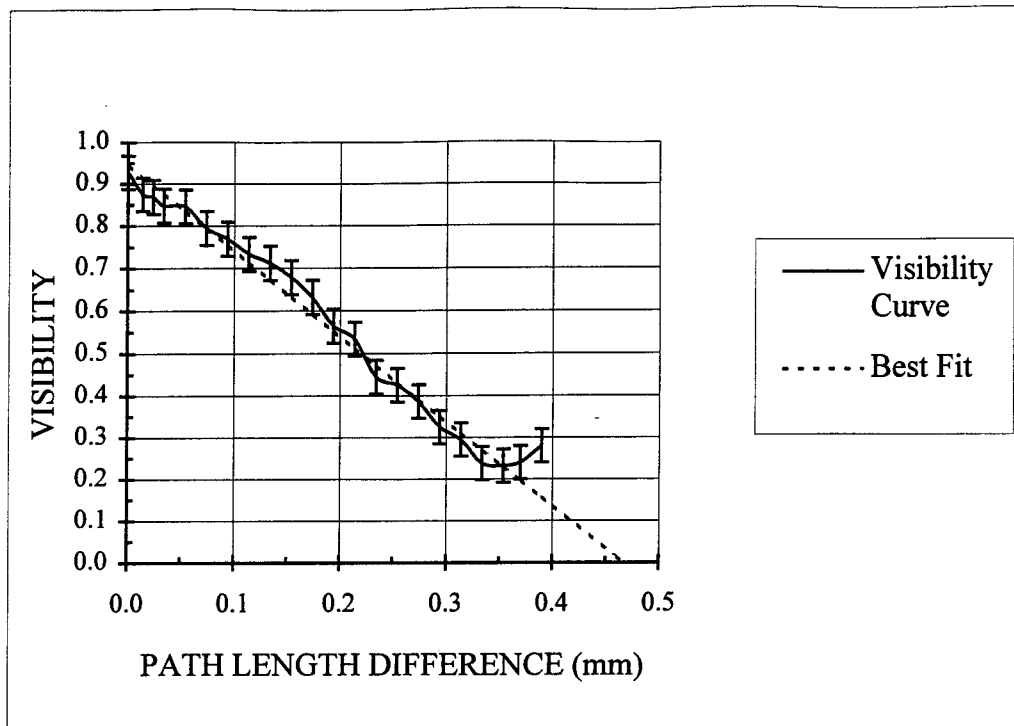
(a)
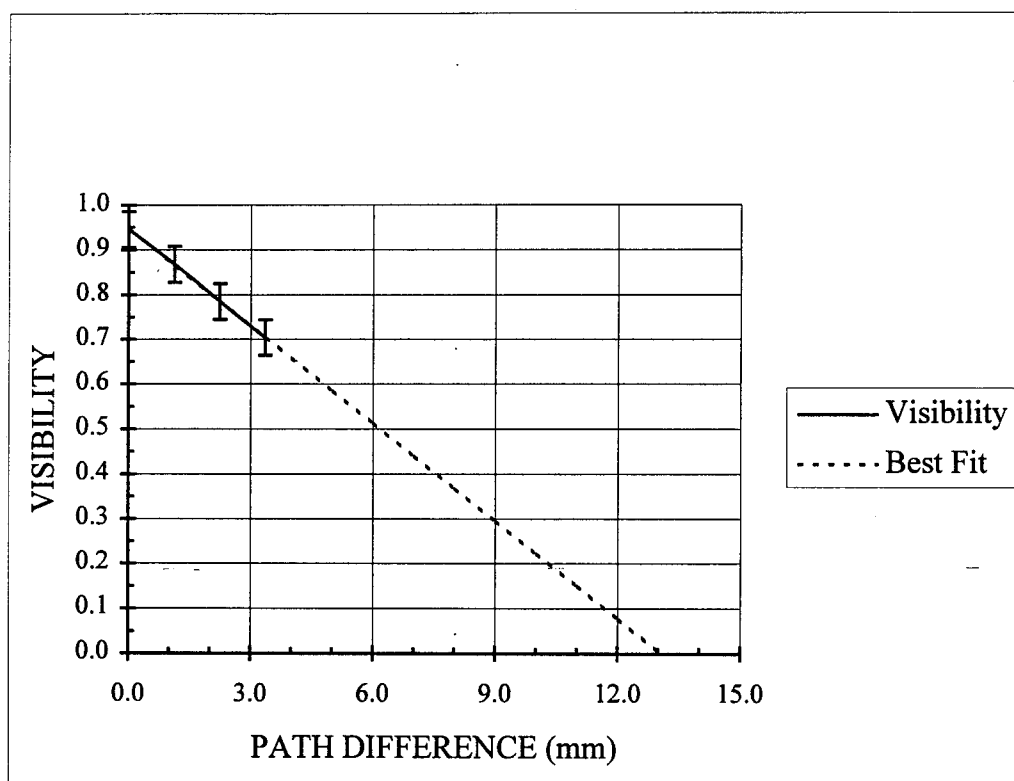
(b)

Figure 15. The visibility curve of the LDA operating at 240 mA (a) and the plot of the visibility curve peaks (b).

curve similar to Figure 5(d). By graphing a line through the visibility curve peaks, one can estimate the path length difference beyond which no interference will occur and the beams are considered incoherent with respect to each other.[46] Due to the physical limitations of translating the mirror of the interferometer, only four peaks of the visibility curve could be measured and graphed. Thus, an extrapolated estimate of the coherence length of the LDA at 240 mA, as graphed in Figure 15(b), was 2.6 ± 0.2 cm.

Far Field Combining of Two Lobes into One Lobe Using an Optical Delay Line

The second phase of experiments investigated the methods and techniques of forming a single-lobe, far-field beam using an optical delay line as a means of maximizing the power density in the far field. The experiment was set up as shown in Figure 13 where the CID was in the far-field plane and the plane mirrors were independently adjustable. Figures 16(a) and 16(b) show the two lobes imaged in the far-field before combination at 200 mA. Then the two lobes were combined in the far-field with no optical delay line to observe the results of interference upon combination. As an example of the observed interference patterns resulting from the far-field recombination of the two lobes, Figure 16(c) shows the maximum interference pattern observed from recombination. The contour and x-axis profile plots in Figure 16(c) clearly show how the two lobes interfered when combined. The two lobes were then combined in the far-field
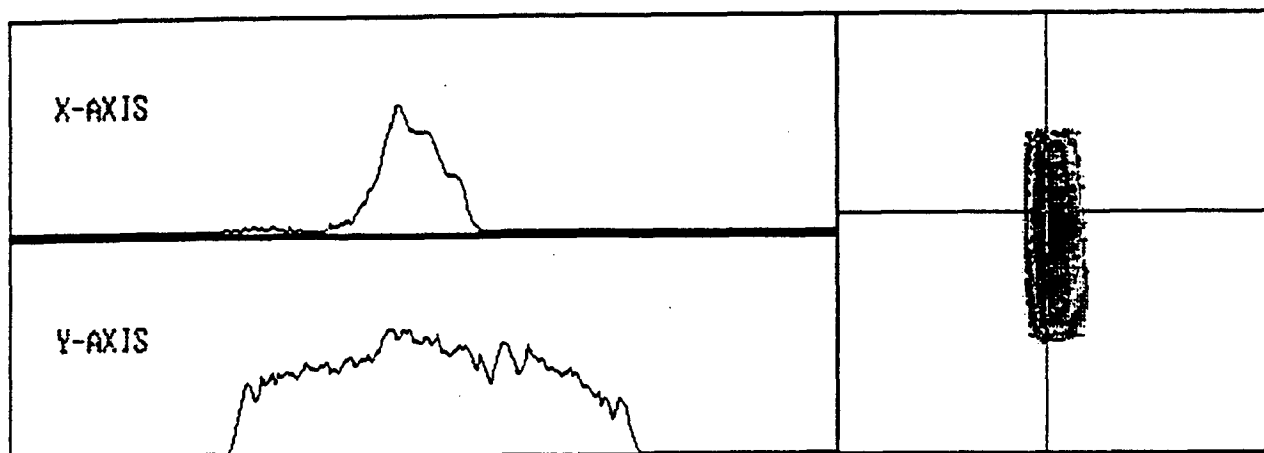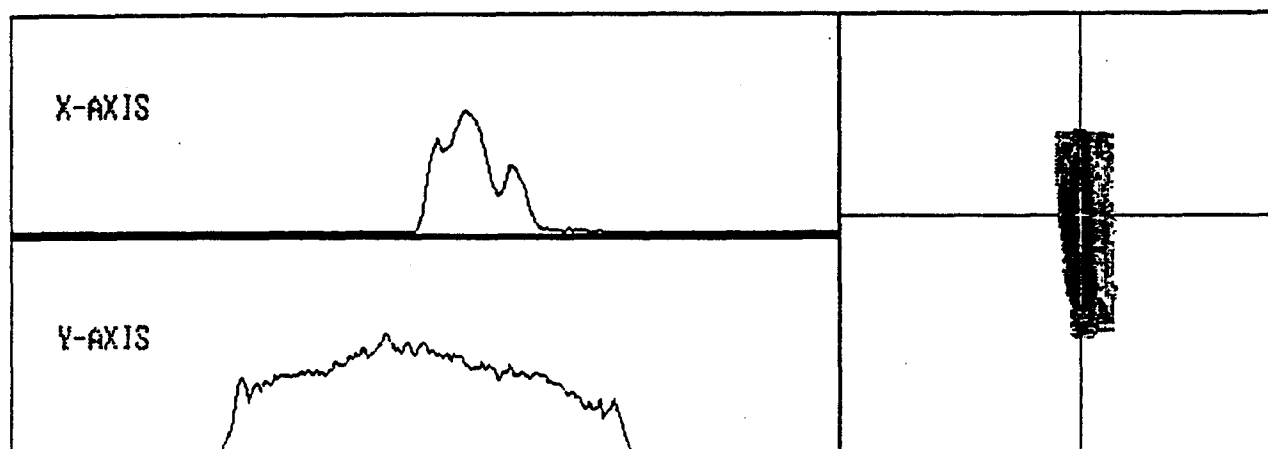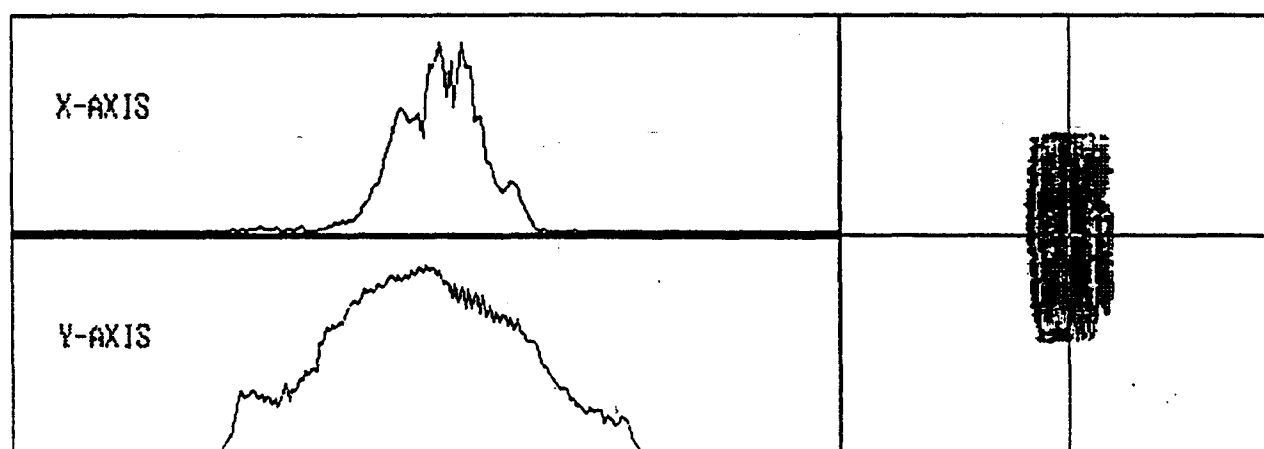
Figure 16. With the LDA operating at 200 mA, the far-field pattern of the right lobe (a), the left lobe (b), and when combined with maximum interference (c).

using two techniques, glass cubes as an optical delay line and a λ/2-wave plate, to produce interference-free, far-field lobes.

Glass Cubes as Optical Delay Line

The two lobes were combined in the far field, as shown in Figure 13, after introducing two glass cubes into the light gray beam immediately before lens $L4$. The glass cubes acted as the optical delay line, equivalent to an optical delay of about 2.5 ± 0.1 cm, to observe their effect upon the combination of the lobes. The cubes were oriented so the linearly polarized light which was parallel to the junction of the array passed through the cubes. The additional path length traveled by the light gray beam when turned by the steering mirror was 0.30 ± 0.05 cm. Thus, the total optical delay introduced into the path of the light gray beam was 2.8 ± 0.2 cm, greater than the estimated value of the coherence length. The relative intensities of the separate lobes and the intensity, FWHM, divergence angle, and the output power of the resultant single-lobe, far-field intensity pattern upon combination were measured for different operating currents.

At an operating current of 200 mA, the two lobes (before combination) appeared as in Figures 17(a) and 17(b) with peak intensities of 139 ± 4 (units of intensity) and 124 ± 4 (units of intensity), respectively. When the two lobes were combined using the glass cubes as the optical delay line, the resultant single-lobe, far-field intensity pattern
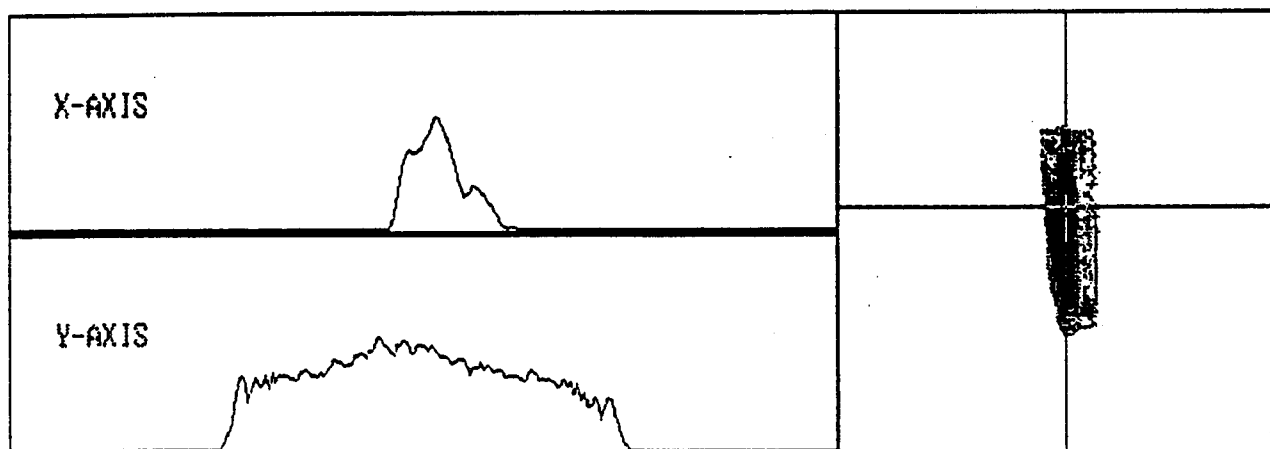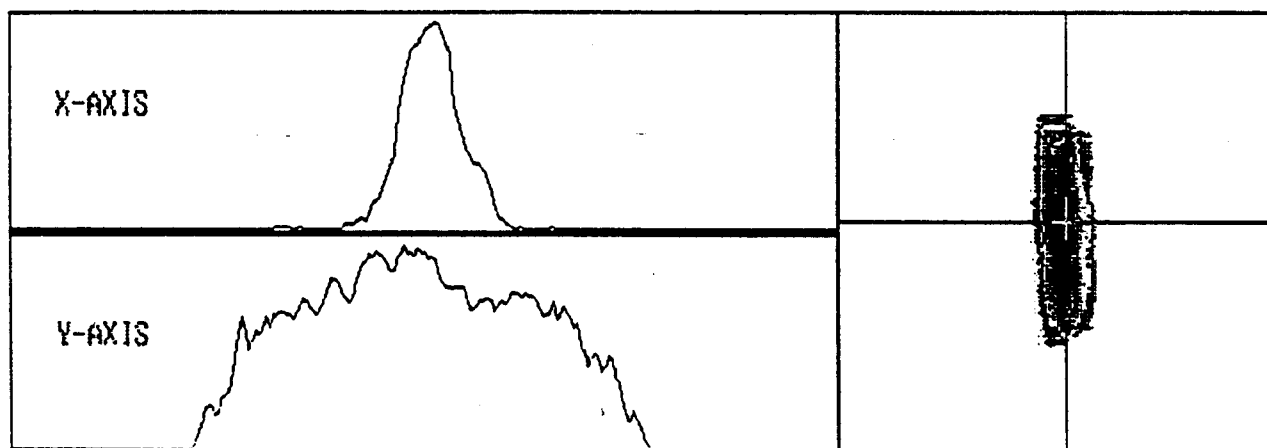
Figure 17. With the LDA operating at 200 mA, the far-field pattern of the right lobe (a), the left lobe (b), and when combined (c).

appeared as in Figure 17(c), with peak intensity of 242 ± 4 (units of intensity), FWHM of 0.59 ± 0.03 mm, divergence angle of 1.65 ± 0.08 degrees (3.4 times the diffraction limit of 0.48 degrees), and output power of 4.3 ± 0.1 mW (80 % of the power exiting the array). The peak intensity of Figure 17(c) is 21 (units of intensity) below the value expected of 263 ± 8 (units of intensity) if the individual lobes combined by incoherent superposition. This indicates the optical delay line was probably not long enough to make the two beams mutually incoherent with respect to each other resulting in some interference. The interference was investigated and observed to be barely observable on the CID, even at maximum interference of the lobes. This is the only instance when the optical delay line did not make the two lobes completely mutually incoherent. The experimental divergence angle does not compare favorably to the theoretical value; however, this is again expected due to the simultaneous operation of several array modes.

The current of the LDA was then increased to 240 mA and the two lobes (before combination) appeared as in Figures 18(a) and 18(b) with peak intensities of 102 ± 4 (units of intensity) and 98 ± 4 (units of intensity), respectively. When the two lobes were combined using the glass cubes as the optical delay line, the resultant single-lobe, far-field intensity pattern appeared as in Figure 18(c), with a peak intensity of 201 ± 4 (units of intensity), FWHM of 0.70 ± 0.03 mm, divergence angle of 1.95 ± 0.09 degrees (4.1 times the diffraction limit), and output power of 18.3 ± 0.7 mW (83 %). The peak intensity of Figure 18(c) is 1 (unit of intensity), right at the expected value of 200 ± 8 (units of intensity) if the individual lobes combined by incoherent superposition. This indicates the optical delay line was long enough to make the two beams mutually
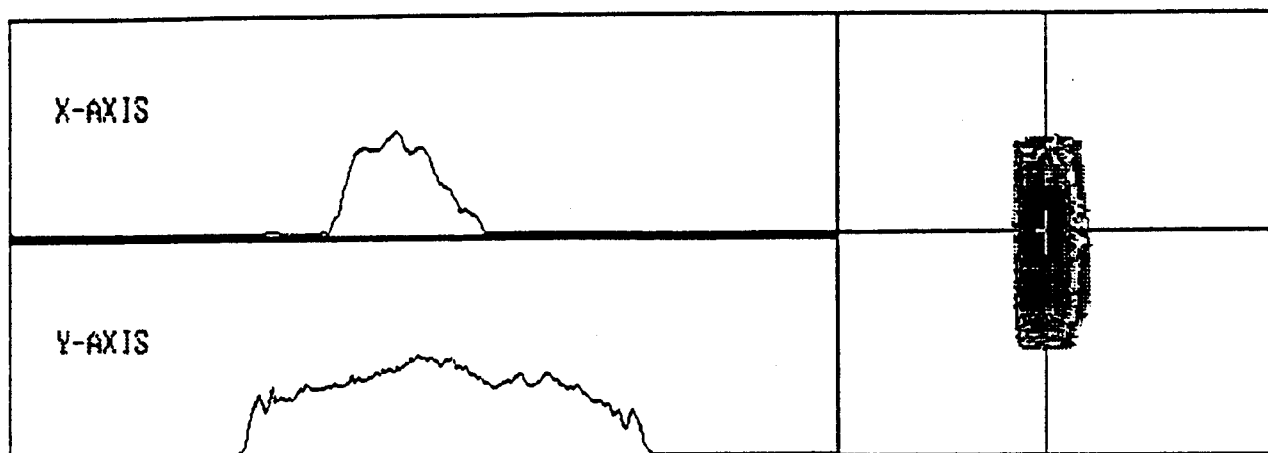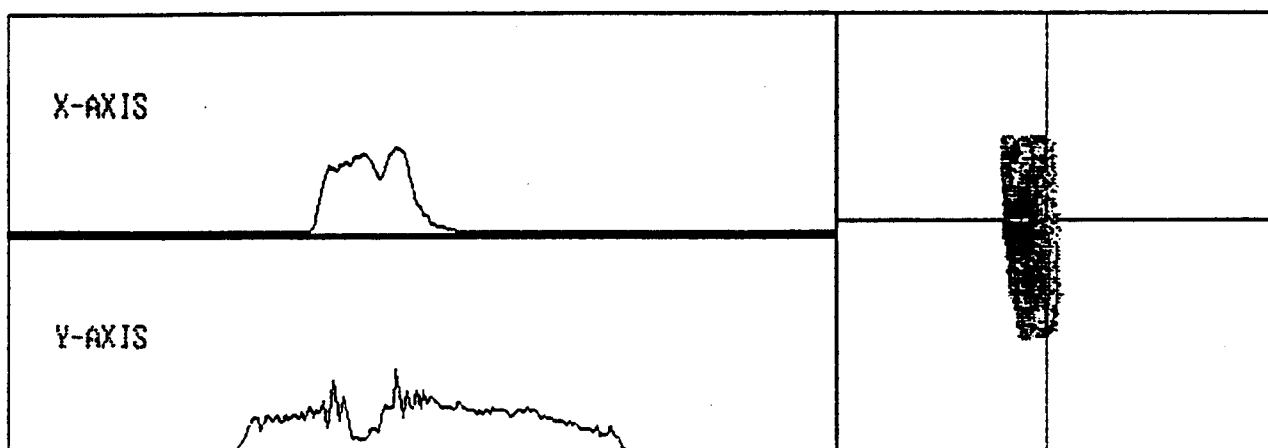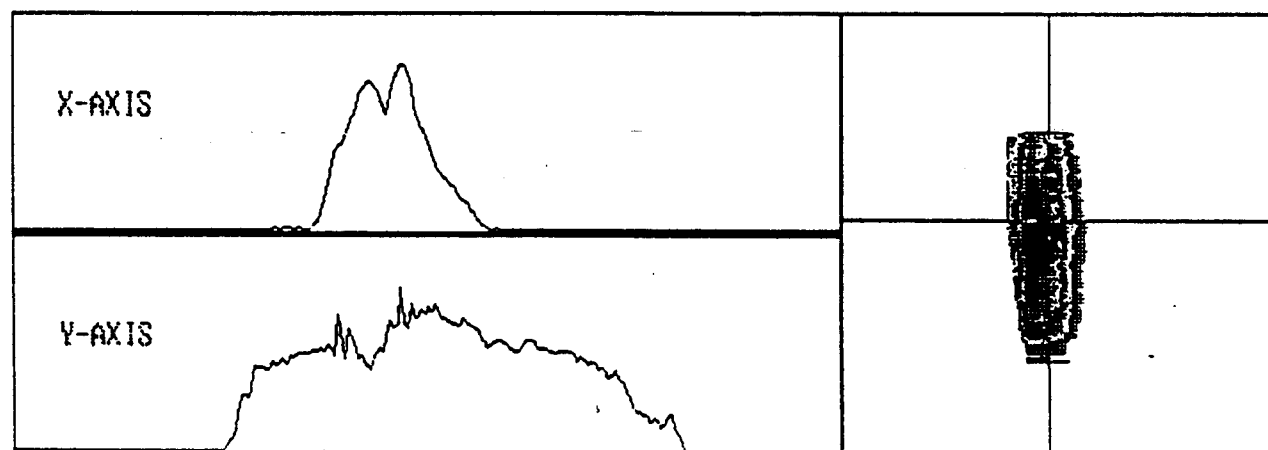
Figure 18. With the LDA operating at 240 mA, the far-field pattern of the right lobe (a), the left lobe (b), and when combined (c).

57

incoherent with respect to each other resulting in no interference and the incoherent superposition of intensities of the individual lobes. The possibility for interference was exhaustively investigated and none was observed on the CID.

The highest operating current investigated, 300 mA, produced the two lobes (before combination) as illustrated in Figures 19(a) and 19(b) with peak intensities of 95 ± 4 (units of intensity) and 152 ± 4 (units of intensity), respectively. When the two lobes were combined using the glass cubes as the optical delay line, the resultant single-lobe, far-field intensity pattern appeared as in Figure 19(c), with peak intensity of 248 ± 5 (units of intensity), FWHM of 0.79 ± 0.04 mm, divergence angle of 2.2 ± 0.1 degrees (4.6 times the diffraction limit), and output power of 37 ± 1 mW (78 %). The peak intensity of Figure 19(c) is 1 (unit of intensity), practically equal to the value expected of 247 ± 8 (units of intensity) if the individual lobes combined by incoherent superposition. This indicates the optical delay line was again long enough to make the two beams mutually incoherent with respect to each other resulting in no interference and the incoherent superposition of intensities of the individual lobes. The possibility for interference was also exhaustively investigated and none was observed on the CID. As expected, the experimental diffraction limit again does not compare favorably to the theoretical value.
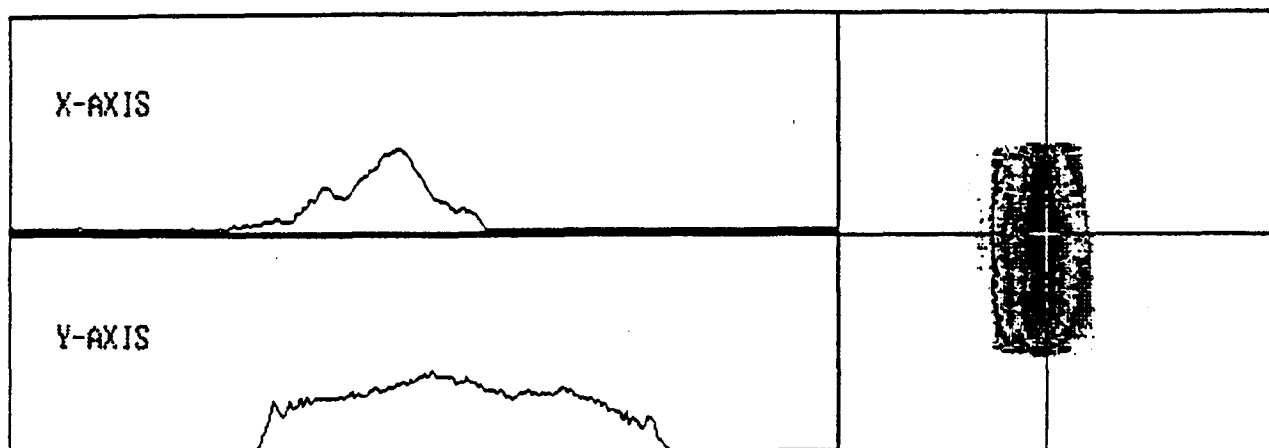
X-AXIS

Y-AXIS

(a)

X-AXIS

Y-AXIS

(b)

X-AXIS

Y-AXIS
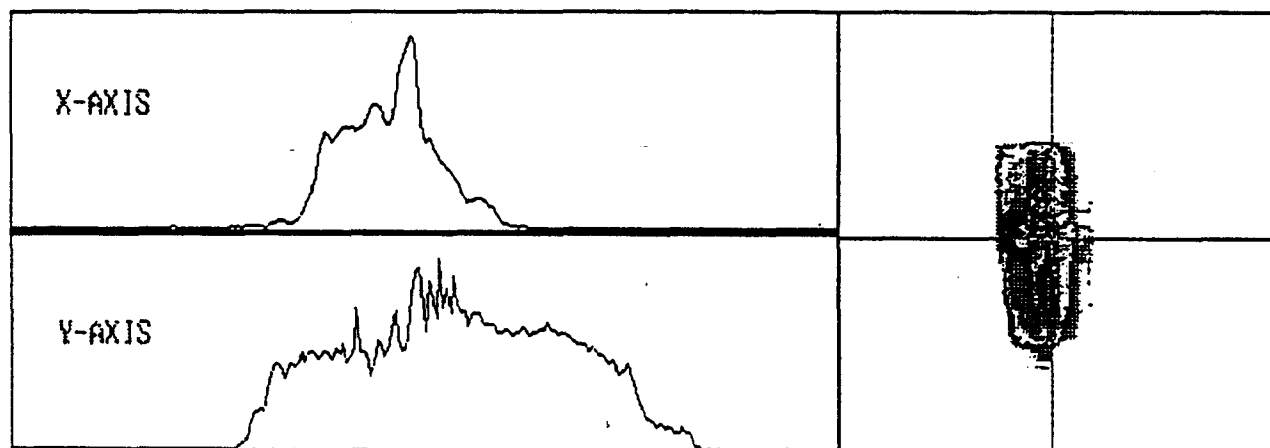
(c)
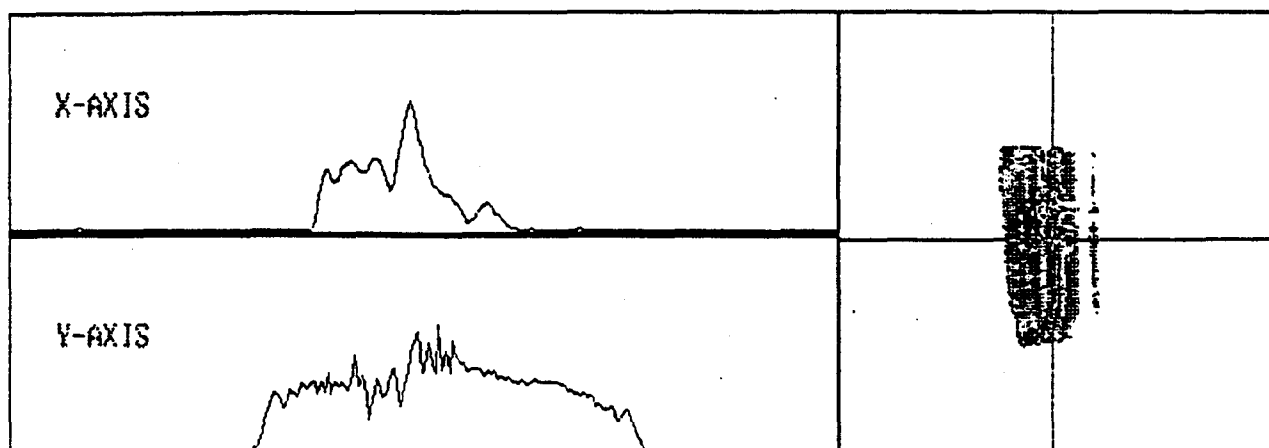
Figure 19. With the LDA operating at 300 mA, the far-field pattern of the right lobe (a), the left lobe (b), and when combined (c).

Half-wave Plate in Place of Optical Delay Line

The two lobes were also combined in the far field, as shown in Figure 13, after introducing a $\lambda/2$-wave plate (designed for $\lambda = 875$ nm, zero order) in place of the optical delay placed immediately before lens *L4*. The $\lambda/2$-wave plate was oriented so the incident linearly polarized light was rotated by 90 degrees with respect to the junction of the array as it passed through the plate. The additional path distance traveled by the light gray beam when turned by the steering mirror was about 0.30 ± 0.05 cm. The peak intensities of the separate lobes and the intensity, FWHM, divergence angle, and the output power of the resultant single-lobe, far-field intensity pattern upon combination were measured for different operating currents.

Just as in the previous case with the glass cubes with the LDA operating at a current of 200 mA, the two lobes (before combination) were the same as those in Figures 17(a) and 17(b) with peak intensities of 139 ± 4 (units of intensity) and 124 ± 4 (units of intensity), respectively. When the two lobes were combined the resultant single-lobe, far-field intensity pattern appeared as in Figure 20(a), with a peak intensity of 255 ± 4 (units of intensity), FWHM of 0.55 ± 0.03 mm, divergence angle of 1.51 ± 0.07 degrees (3.1 times the diffraction limit), and output power of 4.4 ± 0.1 mW (81 %). The relative intensity of Figure 20(a) is 9 (units of intensity) below the value expected of 263 ± 8 (units of intensity) if the individual lobes combined by incoherent superposition, but within experimental error. The possibility of interference was investigated, but none
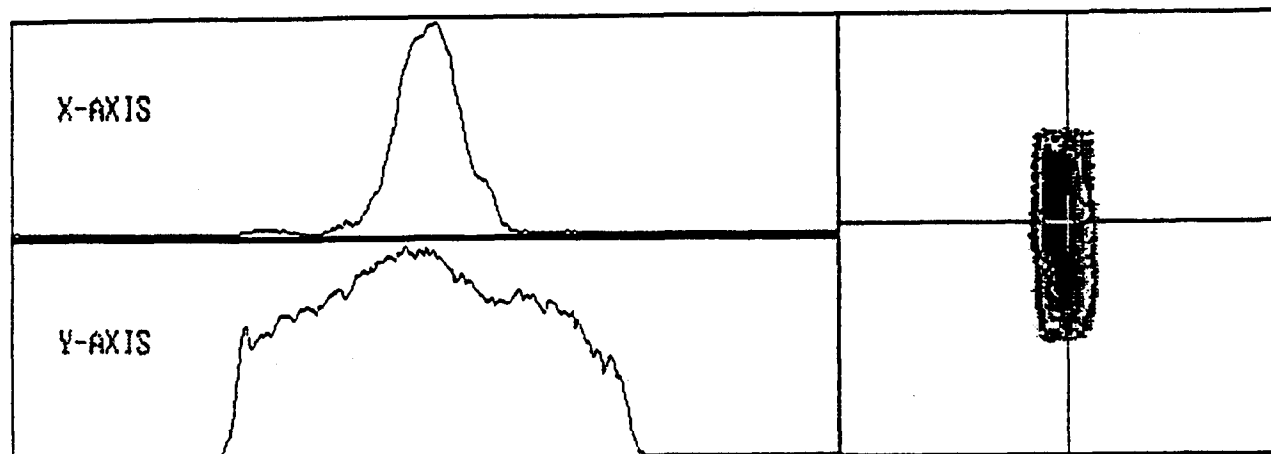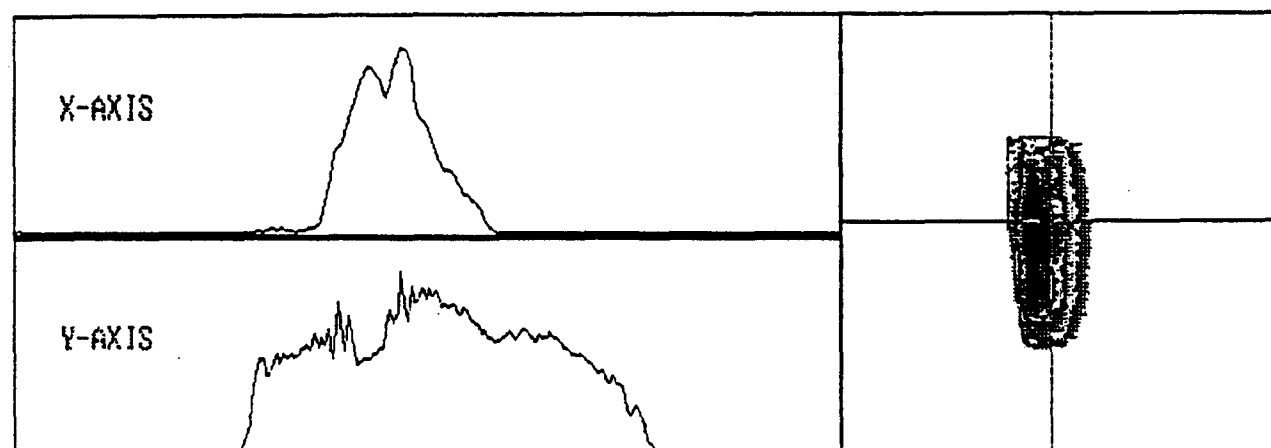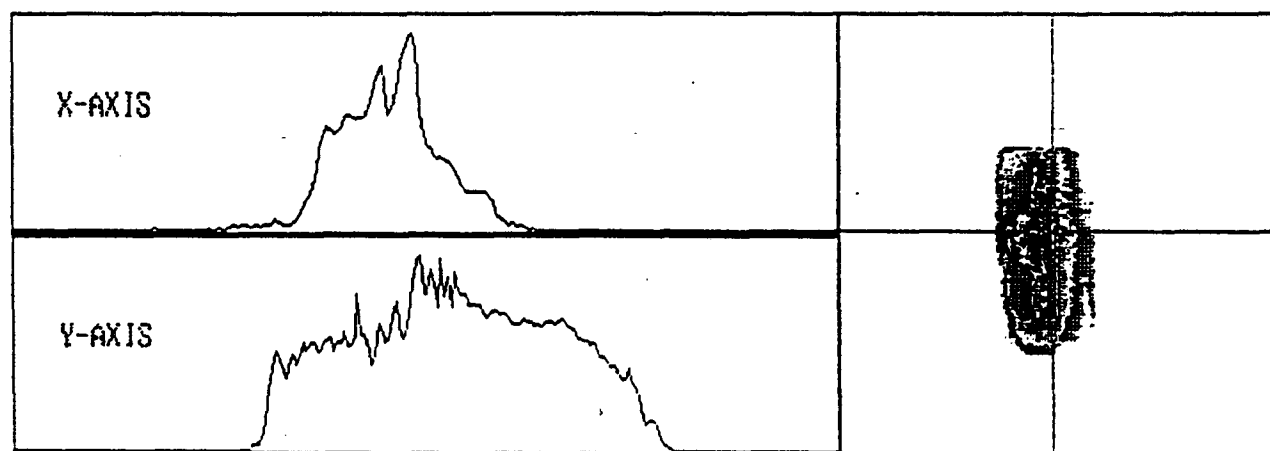
Figure 20. Using the half-wave plate, the combined lobes in the far-field at 200 mA (a), 240 mA (b), and 300 mA (c).

was detected on the CID, even at maximum interference of the lobes. The experimental divergence angle fails to compare favorably to the theoretical value as before.

The two lobes (before combination) shown in Figures 18(a) and 18(b) with peak intensities of 102 ± 4 (units of intensity) and 98 ± 4 (units of intensity), respectively, were produced in the far field when the LDA was operating at 240 mA. When the two lobes were combined using the λ/2-wave plate, the resultant single-lobe, far-field intensity pattern appeared as in Figure 20(b), with a peak intensity of 203 ± 4 (units of intensity), FWHM of 0.78 ± 0.04 mm, divergence angle of 2.2 ± 0.1 degrees (4.5 times the diffraction limit), and output power of 18.50 ± 0.09 mW (84 %). The peak intensity of Figure 18(c) is 3 (units of intensity) above the value expected of 200 ± 8 (units of intensity) if the individual lobes combined by incoherent superposition, within error. This indicates the two beams were made mutually incoherent with respect to each other resulting in no interference and the incoherent superposition of intensities of the individual lobes.

The final experiment was performed at an operating current of 300 mA and produced the two lobes (before combination) as illustrated in Figures 19(a) and 19(b) with peak intensities of 95 ± 4 (units of intensity) and 152 ± 4 (units of intensity), respectively. When the two lobes were combined using the wave plate, the resultant single-lobe, far-field intensity pattern appeared as in Figure 20(c), with a peak intensity of 242 ± 5 (units of intensity), FWHM of 0.92 ± 0.05 mm, divergence angle of 2.6 ± 0.1 degrees (5.4 times the diffraction limit), and output power of 37 ± 1 mW (79 %). The

peak intensity of Figure 20(c) is 5 (units of intensity) below the value expected of

247 ± 8 (units of intensity) if the individual lobes combined by incoherent superposition,

but within the experimental error. This indicates the wave plate made the two beams

mutually incoherent with respect to each other resulting in no interference and the

incoherent superposition of intensities of the individual lobes. The possibility for

interference was checked again and none was observed on the CID. As expected, the

experimental divergence angle again does not compare favorably to the theoretical value.

To summarize the divergence angle results, Figure 21 shows a comparison of the
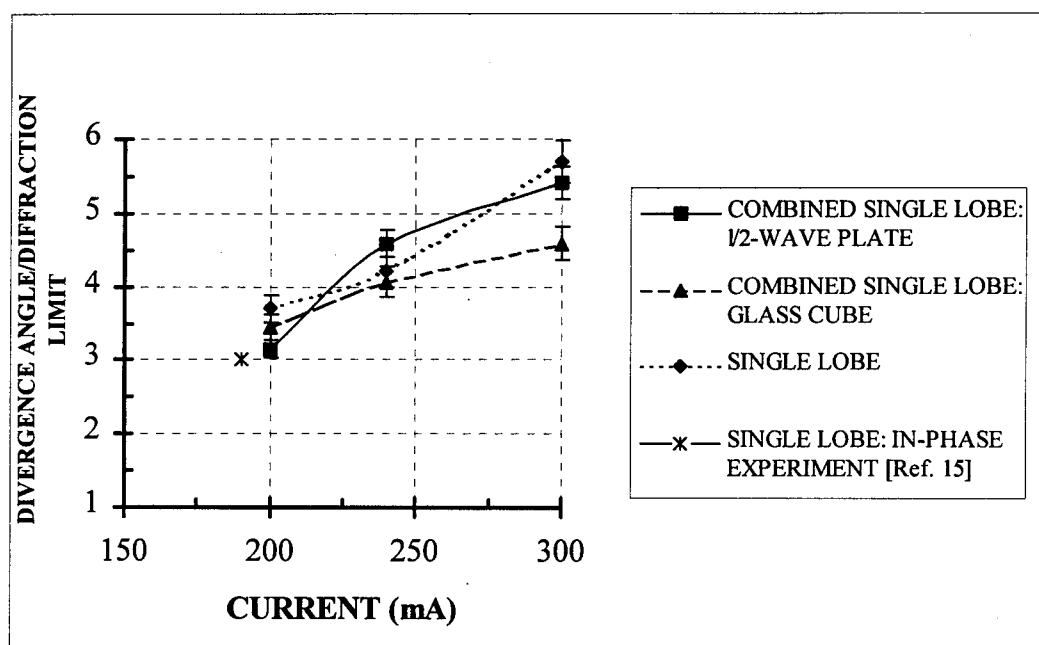
Figure 21. Comparison of divergence angle/diffraction limit versus current.

experimental divergence angle divided by the diffraction limit value versus the operating

current of the LDA. This comparison shows the divergence angle of the single lobes

increases as the current increases; however, the act of forming the single lobes using the

glass cubes and the wave plate did not increase the divergence angle of the resultant

single lobes.

IV. Conclusions and Recommendations

Conclusions

A simple and practical technique to generate a single-lobe, far-field intensity pattern from a monolithic, antiphased, laser diode array by introducing an optical delay line into one of the far field lobes has been demonstrated. In the first phase of the study, the operating parameters and characteristics of the laser diode array in terms of the average output power (including the threshold for lasing), the emission spectra, the beam polarization, and the near- and far-field intensity patterns of the diode were instrumental to the basic understanding of the researcher and served as the basis for the successful completion of combining two far-field lobes into a single-lobe, far-field intensity pattern.

The emission spectra provided vital information about the emitted wavelengths of the LDA, centered about 829 nm and ranging from about 828.3 nm to 830.3 nm at room temperature, and provided insight into the multi-longitudinal modes supported by the laser at different operating currents. The multi-longitudinal mode nature of the laser, which increased at higher operating currents, coupled with the temporal coherence estimates made with the Michelson interferometer, indicated the coherence length of the laser was on the order of several centimeters near threshold and decreased with increasing

current. These facts helped form the first hint that a simple optical delay line introduced into one of the lobes of the two-lobe, far-field intensity pattern would make the two lobes mutually incoherent with respect to each other. Once the lobes were made mutually incoherent, the intensities of the individual lobes added to provide a single-lobe, near-diffraction-limited intensity pattern. The polarization of the laser was observed to be predominately linear and the polarization ratio increased from 2:1 to 94:1 as the current increased from below lasing threshold to 300 mA. This provided the incentive for trying a $\lambda/2$-wave plate. Given the knowledge of the observed near-field intensity pattern, an accurate mathematical model of the near-field electric field was made and enabled the comparison between the expected intensity patterns resulting from rectified, in-phase and out-of-phase near-field profiles. The FWHM of the measured lobes was consistently observed to increase as the current increased. The divergence angles of the lobes, although all above the theoretical value of 0.48 degrees, ranged from 1.51 ± 0.07 degrees to 3.0 ± 0.07 degrees corresponding to 3.1 to 5.4 times the theoretical diffraction limit. The separation angle between the peaks of the two lobes were found to range from 5.3 ± 0.3 degrees to 6.7 ± 0.3 degrees and also increased as the operating current increased. The spatial coherence of the output beams was found to be high in the plane normal to the junction of the array and poor (less than $V = 0.20$) in the plane parallel to the junction.

In the second phase of the study, the methods and techniques of forming a single-lobe, far-field beam using an optical delay line were investigated. First, the two lobes in

the far-field were combined with no optical delay line to observe the results of interference upon combination. Then, the two lobes in the far-field were combined using glass cubes and a λ/2-wave plate to observe the results upon recombination. In every recombination experiment, except when the glass cubes were used as the optical delay line with the LDA operating at 200 mA, the optical delay line successfully made the two far-field lobes mutually incoherent with respect to each other and the intensities of the individual lobes added upon recombination. The exception was due to introducing an optical delay length that was too short to make the lobes mutually incoherent with respect to each other. The output powers achieved ranged from 78-84 percent of the power exiting the array and could have been significantly improved by using optics designed and antireflection coated for the laser wavelength.

The two methods achieved comparable results upon recombining the two lobes into a single lobe, except in the previously mentioned case, but each has advantages and disadvantages. The glass cubes as an optical delay line has the advantage recombining the two lobes in the far field without adversely affecting the polarization of the resultant single-lobe, intensity pattern. Unfortunately, as evidenced in the 200 mA experiment, the optical delay line must be sufficiently long to ensure the lobes are mutually incoherent. The problem of ensuring the path length difference is beyond the coherence length of the lobes can be easily overcome by introducing a longer optical delay line. On the other hand, the λ/2-wave plate has the advantage of rotating the polarization at any current, but its effectiveness in making the two lobes mutually incoherent depends directly upon the

lobes being linearly polarized. Also, by rotating the polarization of one of the lobes, when the two lobes are recombined, they no longer are in their initial state of polarization.

This technique compares favorably with more elaborate schemes previously performed using integrated phase plates, phase conjugation, etc., and has the potential to double the usable power from similar laser diode arrays. The experiments performed demonstrate this method is directly applicable to one-dimensional laser diode arrays and could be adapted for use with two-dimensional arrays as well.

Recommendations

First, since the concept of using an optical delay line to recombine the two lobes in the far field with their intensities adding in a single-lobe, far-field intensity pattern has been proven, the potential for immediate military and industrial use shows great promise due to the simple methods involved. Applications should be immediately explored as outlined in the introduction. Second, during the course of this study, the observation that the lobes and elements did not interfere in the plane of low spatial coherence when passed through the interferometer, indicates more careful study and further investigation is warranted.

Appendix A: Far-field Intensity Pattern Calculated from Rectified, In-phase Near Field

It is assumed the near-field electric-field distribution for a rectified, in-phase laser diode array mode with an even number of elements can be represented as:

$$E_{NF(In-phase)}(x) = E_{NF}(0) \cdot \left| \sin\left([2\pi] \frac{x}{2b} \right) \right| \cdot Gaus\left(\frac{x}{a} \right), \qquad \text{(A-1)}$$

where

$$Gaus\left(\frac{x}{a} \right) = \exp\left[-\pi \left(\frac{x}{a} \right)^2 \right], \qquad \text{(A-2)}$$

$E_{NF}(0)$ is the peak electric field amplitude at the center of the LDA, x is the lateral displacement from the center of the array along the junction axis, b is the center-to-center distance between array elements, and a is the width of the Gaussian determined from the actual near-field intensity profile, approximates the combined out-of-phase near-field wave front. (Note: For an array with an odd number of elements, replace the sine function in Equation (A-1) with a cosine function.)

The Fourier transform of the near-field rectified, in-phase electric-field distribution gives the far-field rectified, in-phase electric-field distribution. Thus:

69

$$E_{FF}(\upsilon) = \mathfrak{I}\left\{E_{NF(In-phase)}(x)\right\}$$

$$= \mathfrak{I}\left\{E_{NF(In-phase)}(0)\cdot\left|\sin\left(2\pi\frac{x}{2b}\right)\right|\cdot Gaus\left(\frac{x}{a}\right)\right\} \quad , \quad \text{(A-3)}$$

where

$$\upsilon = \left(\frac{x_f}{\lambda f}\right), \qquad \text{(A-4)}$$

and x_f is the horizontal axis coordinate in the focal plane, λ is the wavelength, and f is the focal length of the lens used for far field generation. To simplify the calculations, first consider the Fourier transform in Equation (A-3) as a single half-period of the cosine function. This gives:

$$t_1(x) = \cos\left(2\pi\frac{x}{2b}\right)\cdot rect\left(\frac{x}{b}\right), \qquad \text{(A-5)}$$

where

$$rect\left(\frac{x-x_0}{b}\right) = \begin{cases} 0, & \left|\dfrac{x-x_0}{b}\right| > \dfrac{1}{2} \\[2ex] \dfrac{1}{2}, & \left|\dfrac{x-x_0}{b}\right| = \dfrac{1}{2} \\[2ex] 1, & \left|\dfrac{x-x_0}{b}\right| < \dfrac{1}{2} \end{cases} \qquad \text{(A-6)}$$

The Fourier transform of Equation (A-5) can be simplified using the identity:

$$\mathfrak{I}\{g(x)\cdot h(x)\} = \mathfrak{I}\{g(x)\} * \mathfrak{I}\{h(x)\}, \qquad \text{(A-7)}$$

and the following Fourier transforms:

$$\Im\left\{\cos\left(2\pi\frac{x}{2b}\right)\right\} = \frac{1}{2}\left[\delta\left(\upsilon - \frac{1}{2b}\right) + \delta\left(\upsilon + \frac{1}{2b}\right)\right],\qquad\text{(A-8)}$$

and

$$\Im\left\{rect\left(\frac{x}{b}\right)\right\} = |b|\,\text{sinc}(b\upsilon),\qquad\text{(A-9)}$$

where

$$\text{sinc}\left(\frac{x - x_0}{b}\right) = \frac{\sin\left[\pi\left(\dfrac{x - x_0}{b}\right)\right]}{\pi\left(\dfrac{x - x_0}{b}\right)}.\qquad\text{(A-10)}$$

Thus, the Fourier transform of a half-period of a cosine function is:

$$\Im\left\{t_1(x)\right\} = \Im\left\{\cos\left(2\pi\frac{x}{2b}\right)\right\} * \Im\left\{rect\left(\frac{x}{b}\right)\right\}$$

$$= \frac{1}{2}\left[\delta\left(\upsilon - \frac{1}{2b}\right) + \delta\left(\upsilon + \frac{1}{2b}\right)\right] * |b|\,\text{sinc}(b\upsilon).\qquad\text{(A-11)}$$

$$= \frac{|b|}{2}\left[\text{sinc}\left(b\upsilon - \frac{1}{2}\right) + \text{sinc}\left(b\upsilon + \frac{1}{2}\right)\right]$$

Similarly, the fully rectified cosine function, $t_2(x)$, can be written as the sum of offset cosine half-periods; i.e., :

$$t_2(x) = \sum_{n=-\infty}^{\infty} \cos\left(2\pi \frac{x+bn}{2b}\right) \cdot rect\left(\frac{x+bn}{b}\right)$$

$$= \sum_{n=-\infty}^{\infty} \int_{-\infty}^{\infty} \cos\left(2\pi \frac{\alpha}{2b}\right) \cdot rect\left(\frac{\alpha}{b}\right) \cdot \delta\left[\alpha - (x+bn)\right] d\alpha$$

$$= \int_{-\infty}^{\infty} \cos\left(2\pi \frac{\alpha}{2b}\right) \cdot rect\left(\frac{\alpha}{b}\right) \sum_{n=-\infty}^{\infty} \delta\left[\alpha - (x+bn)\right] d\alpha \qquad . \qquad \text{(A-12)}$$

$$= \int_{-\infty}^{\infty} \cos\left(2\pi \frac{\alpha}{2b}\right) \cdot rect\left(\frac{\alpha}{b}\right) \left|\frac{1}{b}\right| comb\left(\frac{x-\alpha}{b}\right) d\alpha$$

$$= \left[\cos\left(2\pi \frac{x}{2b}\right) \cdot rect\left(\frac{x}{b}\right)\right] * \left|\frac{1}{b}\right| comb\left(\frac{x}{b}\right)$$

The Fourier transform of $t_2(x)$, given in Equation (A-12), is solved using the identity:

$$\Im\{g(x) * h(x)\} = \Im\{g(x)\} \cdot \Im\{h(x)\}, \qquad \text{(A-13)}$$

the Fourier transform of the comb function:

$$\Im\left\{\left|\frac{1}{b}\right| comb\left(\frac{x}{b}\right)\right\} = \Im\{comb(b\upsilon)\}, \qquad \text{(A-14)}$$

and Equation (A-11). The Fourier transform of $t_2(x)$, the fully rectified cosine function, in Equation (A-12) is thus:

$$\Im\{t_2(x)\} = \Im\left\{\left[\cos\left(2\pi \frac{x}{2b}\right) \cdot rect\left(\frac{x}{b}\right)\right]\right\} * \Im\left\{\left|\frac{1}{b}\right| comb\left(\frac{x}{b}\right)\right\}$$

$$= \frac{|b|}{2}\left[sinc\left(b\upsilon - \frac{1}{2}\right) + sinc\left(b\upsilon + \frac{1}{2}\right)\right] \cdot comb(b\upsilon) \qquad . \qquad \text{(A-15)}$$

$$= \frac{1}{2}\left[sinc\left(b\upsilon - \frac{1}{2}\right) + sinc\left(b\upsilon + \frac{1}{2}\right)\right] \cdot \sum_{n=-\infty}^{\infty} \delta\left(\upsilon - \frac{n}{b}\right)$$

The Fourier transform of the fully rectified sine function is equivalent to:

$$\Im\left\{\left|\sin\left(2\pi\frac{x}{2b}\right)\right|\right\} = \Im\left\{\left|\cos\left(2\pi\frac{x}{2b}-\frac{b}{2}\right)\right|\right\} = \Im\left\{t_2\left(x-\frac{b}{2}\right)\right\}. \qquad \text{(A-16)}$$

Using the following identity:

$$\Im\left\{f\left(x-x_0\right)\right\} = e^{-j2\pi\,x_0\,\upsilon}\,\Im\left\{t_2(x)\right\}, \qquad \text{(A-17)}$$

the Fourier transform of Equation (A-16), the complete rectified sine function, is:

$$\Im\left\{\left|\sin\left(2\pi\frac{x}{2b}\right)\right|\right\} = e^{-j2\pi\,\frac{b}{2}\upsilon}\,\Im\left\{t_2(x)\right\}. \qquad \text{(A-18)}$$

To make the far-field electric field calculations realistic, the near-field electric field distribution in Equation (A-1) can be rewritten as:

$$E_{NF(In-phase)}(x) = E_{NF}(0)\cdot t_2\left(x-\frac{b}{2}\right)\cdot Gaus\left(\frac{x}{a}\right), \qquad \text{(A-19)}$$

and substituting this equation in Equation (A-3) gives the far-field electric field as:

$$E_{FF}(\upsilon) = \Im\left\{E_{NF(In-phase)}(x)\right\}$$
$$= \Im\left\{E_{NF}(0)\cdot t_2\left(x-\frac{b}{2}\right)\cdot Gaus\left(\frac{x}{a}\right)\right\}. \qquad \text{(A-20)}$$

To find $E_{FF}(v)$, use the identity in Equation (A-7), the Fourier transform from Equation (A-15), and Fourier transform of the Gaussian function in Equation (A-21):

$$\Im\left\{Gaus\left(\frac{x}{a}\right)\right\} = |a|\,Gaus(a\upsilon).$$
(A-21)

This gives the far-field, rectified, in-phase electric field distribution as:

$$\frac{E_{FF}(\upsilon)}{E_{NF}(0)} = \Im\left\{t_2\left(x-\frac{b}{2}\right)\right\}\cdot \Im\left\{Gaus\left(\frac{x}{a}\right)\right\}$$

$$= \left\{e^{-j\pi b\upsilon}\frac{|b|}{2}\left[sinc\left(b\upsilon-\frac{1}{2}\right)+sinc\left(b\upsilon+\frac{1}{2}\right)\right]\cdot comb(b\upsilon)\right\}*|a|\,Gaus(a\upsilon)$$

$$= \left\{e^{-j\pi b\upsilon}\frac{1}{2}\left[sinc\left(b\upsilon-\frac{1}{2}\right)+sinc\left(b\upsilon+\frac{1}{2}\right)\right]\cdot \sum_{n=-\infty}^{\infty}\delta\left(\upsilon-\frac{n}{b}\right)\right\}*|a|\,Gaus(a\upsilon)$$

$$= \sum_{n=-\infty}^{\infty}e^{-j\pi b\alpha}\frac{1}{2}\int_{-\infty}^{\infty}\left[sinc\left(b\alpha-\frac{1}{2}\right)+sinc\left(b\alpha+\frac{1}{2}\right)\right]\cdot\delta\left(\alpha-\frac{n}{b}\right)\cdot|a|\,Gaus(a(\upsilon-\alpha))d\alpha$$

$$= \sum_{n=-\infty}^{\infty}e^{-j\pi n}\frac{1}{2}\left[sinc\left(n-\frac{1}{2}\right)+sinc\left(n+\frac{1}{2}\right)\right]\cdot|a|\,Gaus\left(a\left(\upsilon-\frac{n}{b}\right)\right)$$

$$= \sum_{n=-\infty}^{\infty}(-1)^n\frac{1}{2}\left[sinc\left(n-\frac{1}{2}\right)+sinc\left(n+\frac{1}{2}\right)\right]\cdot|a|\,Gaus\left(a\left(\upsilon-\frac{n}{b}\right)\right).$$
(A-22)

Rewriting Equation (A-22) in terms of the far-field electric field distribution in the center

of the far-field distribution, i.e., $\nu = 0$ in the denominator of Equation (A-23),yields:

$$\frac{E_{FF}(\upsilon)}{E_{FF}(0)} = \left[\frac{\displaystyle\sum_{n=-\infty}^{\infty}(-1)^n\frac{1}{2}\left[sinc\left(n-\frac{1}{2}\right)+sinc\left(n+\frac{1}{2}\right)\right]\cdot|a|\,Gaus\left(a\left(\upsilon-\frac{n}{b}\right)\right)}{\displaystyle\sum_{n=-\infty}^{\infty}(-1)^n\frac{1}{2}\left[sinc\left(n-\frac{1}{2}\right)+sinc\left(n+\frac{1}{2}\right)\right]\cdot|a|\,Gaus\left(a\left(\frac{n}{b}\right)\right)}\right].$$
(A-23)

The rectified, in-phase far-field intensity pattern is then just the square of the far-field electric field distribution given in Equation (A-23), namely:

$$
\frac{I_{FF}(\upsilon)}{I_{FF}(0)} = \left| \frac{\sum_{n=-\infty}^{\infty}(-1)^n \frac{1}{2}\left[\mathrm{sinc}\left(n-\frac{1}{2}\right)+\mathrm{sinc}\left(n+\frac{1}{2}\right)\right]\cdot |a|\,Gaus\left(a\left(\upsilon-\frac{n}{b}\right)\right)}{\sum_{n=-\infty}^{\infty}(-1)^n \frac{1}{2}\left[\mathrm{sinc}\left(n-\frac{1}{2}\right)+\mathrm{sinc}\left(n+\frac{1}{2}\right)\right]\cdot |a|\,Gaus\left(a\left(\frac{n}{b}\right)\right)} \right|^2
$$

$$
= \left| \frac{\sum_{n=-\infty}^{\infty}(-1)^n\left[\mathrm{sinc}\left(n-\frac{1}{2}\right)+\mathrm{sinc}\left(n+\frac{1}{2}\right)\right]\cdot Gaus\left(a\left(\upsilon-\frac{n}{b}\right)\right)}{\sum_{n=-\infty}^{\infty}(-1)^n\left[\mathrm{sinc}\left(n-\frac{1}{2}\right)+\mathrm{sinc}\left(n+\frac{1}{2}\right)\right]\cdot Gaus\left(a\left(\frac{n}{b}\right)\right)} \right|^2 . \qquad \text{(A-24)}
$$

Figure 3(b) is a plot of the modulus squared of Equation (A-22) with $b = 10$ μm, $a = 100$ μm, and $n = $ -5, -4, ..., 4, 5 giving the unnormalized, far-field intensity pattern.

Note: For an array with an odd number of elements, this operation gives similar results, except Equation (A-23) would not have the $(-1)^n$ coefficient.[19, 47]

Appendix B: Far-field Intensity Pattern Calculated from Out-of-phase Near Field

The near-field electric-field distribution for an out-of-phase laser diode array

mode with an even number of elements may be represented as :

$$E_{NF(Out-of-phase)}(x) = E_{NF}(0) \cdot \sin\left(\left[2\pi\right]\frac{x}{2b}\right) \cdot Gaus\left(\frac{x}{a}\right), \qquad \text{(B-1)}$$

where

$$Gaus\left(\frac{x}{a}\right) = \exp\left[-\pi\left(\frac{x}{a}\right)^2\right], \qquad \text{(B-2)}$$

$E_{NF}(0)$ is the peak electric field amplitude at the center of the LDA, x is the lateral

displacement from the center of the array along the junction axis, b is the center-to-center

distance between array elements, and a is the width of the Gaussian determined from the

actual near-field intensity profile, approximates the combined out-of-phase near-field

wave front. (Note: For an array with an odd number of elements, replace the sine

function in Equation (B-1) with a cosine function.)

The Fourier transform of the near-field out-of-phase electric-field distribution

gives the far-field out-of-phase electric-field distribution. Thus:

$$E_{FF}(\upsilon) = \Im\left\{E_{NF(Out-of-phase)}(x)\ \right\}$$

$$= \Im\left\{E_{NF(Out-of-phase)}(0)\cdot\sin\left(2\pi\,\frac{x}{2b}\right)\cdot Gaus\left(\frac{x}{a}\right)\right\}, \qquad \text{(B-3)}$$

where

$$\upsilon = \left(\frac{x_f}{\lambda f}\right), \qquad \text{(B-4)}$$

and x_f is the horizontal axis coordinate in the focal plane, λ is the wavelength, and f is the focal length of the lens used for far field generation.

The Fourier transform of Equation (B-3) can be simplified using the identity:

$$\Im\{g(x)\cdot h(x)\} = \Im\{g(x)\} * \Im\{h(x)\}, \qquad \text{(B-5)}$$

and the following Fourier transforms:

$$\Im\left\{\sin\left(2\pi\,\frac{x}{2b}\right)\right\} = \frac{1}{2j}\left[\delta\left(\upsilon - \frac{1}{2b}\right) - \delta\left(\upsilon + \frac{1}{2b}\right)\right], \qquad \text{(B-6)}$$

and

$$\Im\left\{Gaus\left(\frac{x}{a}\right)\right\} = |a|\,Gaus(a\upsilon). \qquad \text{(B-7)}$$

This gives the far-field out-of-phase electric-field distribution as:

$$\frac{E_{FF}(\upsilon)}{E_{NF}(0)} = \Im\left\{\sin\left(2\pi\,\frac{x}{2b}\right)\right\} \cdot \Im\left\{Gaus\left(\frac{x}{a}\right)\right\}$$

$$= \frac{1}{2j}\left[\delta\left(\upsilon - \frac{1}{2b}\right) - \delta\left(\upsilon + \frac{1}{2b}\right)\right] * |a|\,Gaus(a\upsilon)$$

$$= \frac{1}{2j}\int_{-\infty}^{\infty}\left[\delta\left(\alpha - \frac{1}{2b}\right) - \delta\left(\alpha + \frac{1}{2b}\right)\right]\cdot|a|\,Gaus(a(\upsilon - \alpha))\,d\alpha$$

$$= \frac{|a|}{2j}\left[Gaus\left(a\left(\upsilon - \frac{1}{2b}\right)\right) - Gaus\left(a\left(\upsilon + \frac{1}{2b}\right)\right)\right]. \qquad \text{(B-8)}$$

Rewriting Equation (B-8) in terms of the far-field out-of-phase electric-field distribution in the center of the far-field distribution, i.e., $\nu = 1/2b$ in the denominator of Equation (B-9), yields:

$$\frac{E_{FF}(\upsilon)}{E_{FF}\left(\frac{1}{2b}\right)} = \left[\frac{\frac{|a|}{2j}\left[Gaus\left(a\left(\upsilon - \frac{1}{2b}\right)\right) - Gaus\left(a\left(\upsilon + \frac{1}{2b}\right)\right)\right]}{\frac{|a|}{2j}\left[1 - Gaus\left(a\left(\frac{1}{2b}\right)\right)\right]}\right]. \qquad \text{(B-9)}$$

The far-field out-of-phase intensity pattern is then just the square of the modulus of the far-field out-of-phase electric-field distribution given in Equation (B-9), namely:

$$\frac{I_{FF}(\upsilon)}{I_{FF}(0)} = \left[\frac{\frac{|a|}{2j}\left[Gaus\left(a\left(\upsilon - \frac{1}{2b}\right)\right) - Gaus\left(a\left(\upsilon + \frac{1}{2b}\right)\right)\right]}{\frac{|a|}{2j}\left[1 - Gaus\left(a\left(\frac{1}{2b}\right)\right)\right]}\right]^2$$

$$= \left[\frac{\left[Gaus\left(a\left(\upsilon - \frac{1}{2b}\right)\right) - Gaus\left(a\left(\upsilon + \frac{1}{2b}\right)\right)\right]}{\left[1 - Gaus\left(a\left(\frac{1}{2b}\right)\right)\right]}\right]^2. \qquad \text{(B-10)}$$

Figure 3(c) is a plot of the modulus squared of Equation (B-8) with $b = 10$ µm and

$a = 100$ µm giving the unnormalized, far-field out-of-phase intensity pattern.

Note: For an array with an odd number of elements, this operation gives similar

results, but the Gaussian functions in Equation (B-8) would add instead of subtract.[19, 47]

Appendix C: Determination of the Far- and Near-field Intensity Pattern Positions

The position of the far- and near-field intensity positions can be calculated exactly using the ray matrix method and a transmission matrix to relate the input and output rays of an optical system. Assuming the paraxial approximation with all rays, namely $\tan\alpha \approx \sin\alpha \approx \alpha$, consider the input rays emanating from the laser diode array and the optical system output rays given by:

$$Input\ Rays = \begin{pmatrix} x_1 \\ \alpha_1 \end{pmatrix}$$

$$Output\ Rays = \begin{pmatrix} x_2 \\ \alpha_2 \end{pmatrix}, \tag{C-1}$$

where x_1 is the height of the input ray above the optic axis, α_1 is the angle between the input ray and the optic axis, x_2 is the height of the output ray above the optic axis, and α_2 is the angle between the output ray and the optic axis. To relate the two rays, the input and output rays can be written in matrix form as:

$$\begin{pmatrix} x_2 \\ \alpha_2 \end{pmatrix} = \begin{pmatrix} A & B \\ C & D \end{pmatrix} \begin{pmatrix} x_1 \\ \alpha_1 \end{pmatrix}, \tag{C-2}$$

where the ABCD matrix is the transmission matrix relating the rays. After multiplying the matrices in Equation (C-2), the following relations result:

$$x_2 = A x_1 + B \alpha_1$$
$$\alpha_2 = C x_1 + D \alpha_1 .$$

(C-3)

The ABCD transmission matrix determined from Figure C1 or C2 is:

$$\begin{pmatrix} A & B \\ C & D \end{pmatrix} = \begin{pmatrix} 1 & S \\ 0 & 1 \end{pmatrix} \begin{pmatrix} 1 & 0 \\ \frac{-1}{f_2} & 1 \end{pmatrix} \begin{pmatrix} 1 & d \\ 0 & 1 \end{pmatrix} \begin{pmatrix} 1 & 0 \\ \frac{-1}{f_1} & 1 \end{pmatrix} \begin{pmatrix} 1 & L \\ 0 & 1 \end{pmatrix},$$

(C-4)

where the first matrix , reading from left-to-right, is the free-space transmission ray

matrix from lens $L2$, with focal length f_2, to the screen (i.e., the plane of either the far or

near field), the second matrix is the ray matrix for transmission through positive thin lens

$L2$, the third matrix is the free-space transmission ray matrix from $L1$ to $L2$, the fourth

matrix is the ray matrix for positive thin lens $L1$, with focal length f_1, and the fifth matrix

is the free-space transmission ray matrix from the laser diode array to $L1$. After matrix

multiplication, the ABCD transmission matrix becomes:

$$\begin{pmatrix} A & B \\ C & D \end{pmatrix} = \left(\begin{array}{c} \dfrac{(f_2 \cdot f_1 - f_1 \cdot S - d \cdot f_2 + d \cdot S - S \cdot f_2)}{(f_2 \cdot f_1)} \\[2em] -\left(\dfrac{f_1 - d + f_2}{f_2 \cdot f_1} \right) \end{array} \right.$$

$$\left. \begin{array}{c} \dfrac{(L \cdot f_2 \cdot f_1 - L \cdot f_1 \cdot S - L \cdot d \cdot f_2 + L \cdot d \cdot S - L \cdot S \cdot f_2 + f_1 \cdot d \cdot f_2 - f_1 \cdot d \cdot S \mp f_1 \cdot S \cdot f_2)}{(f_2 \cdot f_1)} \\[2em] \dfrac{-(L \cdot f_1 - L \cdot d + L \cdot f_2 + f_1 \cdot d - f_2 \cdot f_1)}{(f_2 \cdot f_1)} \end{array} \right).$$

(C-5)

To find the far-field intensity pattern position as shown in Figure C1, x_2 must be independent of x_1 which implies matrix element A in Equation (C-3) must equal zero.

ARRAY L1   **L2**   **SCREEN**

—OPTIC AXIS

Figure C1. Setup to find the far-field intensity pattern position.

Setting matrix element A in Equation (C-5) equal to zero and solving for S, the distance from $L2$ to the far-field plane, gives:

$$S = -\left(\frac{f_2 \cdot f_1 - d \cdot f_2}{-f_1 + d - f_2} \right).$$ (C-6)

Notice S does not depend on L, the distance between the array and $L1$. To find the angular magnification in the far-field plane, matrix element D in Equation (C-5) equals

the ratio of $\dfrac{\alpha_2}{\alpha_1}$.

To find the near-field intensity pattern position as shown in Figure C2, x_2 must be independent of α_1 which implies matrix element B in Equation (C-3) must equal zero.
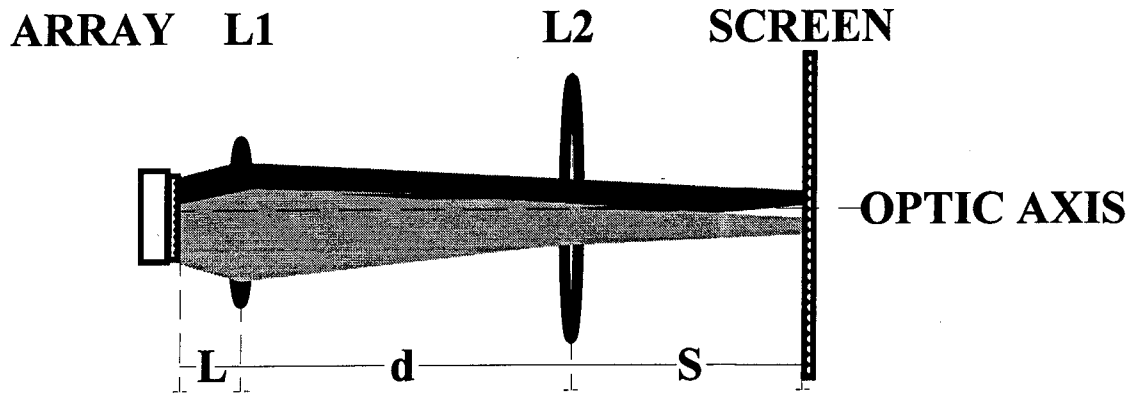
Setting matrix element B in Equation (C-5) equal to zero and solving for S, now the

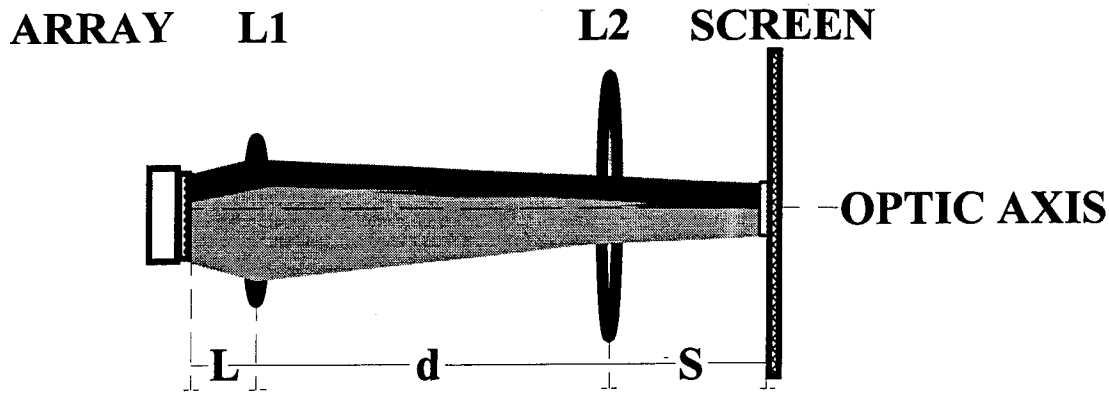ARRAY   L1   L2   SCREEN

−−OPTIC AXIS

Figure C2. Setup to find the near-field intensity pattern position.

distance from *L2* to the near-field plane, gives:

$$S = -\left(\frac{L \cdot f_2 \cdot f_1 - L \cdot d \cdot f_2 + f_1 \cdot d \cdot f_2}{-L \cdot f_1 + L \cdot d - L \cdot f_2 - f_1 \cdot d + f_2 \cdot f_1} \right). \qquad \text{(C-7)}$$

Note, to determine the near-field intensity pattern position, S does depend on L.

For an example, let $f_1 = 0.8$ cm (a $20\times$ objective lens), $f_2 = 15.0$ cm, $L = 0.8$ cm, and $d = 20.0$ cm. For optical systems set up as in Figures C1 and C2, the far- and near-field intensity pattern positions are at $S = 68.6$ cm and $S = 16.4$ cm, respectively.

Note: Since it is sometimes difficult to measure the optical distances precisely, an excellent check to ensure one is viewing the far-field intensity pattern is to check the intensity and width of the pattern as the source is slightly translated back and forth along the optic axis. If the intensity and width of the pattern remains approximately constant as the source is moved, the detector is in the far-field plane.

Bibliography

1.   Geusic, Joseph, W. B. Bridges, and J. I. Pankove. "Coherent Optical Sources for Communications," *Proc. IEEE,* 58: 1419-1439 (October 1970).

2.   Leggett, Kate. "DIAL-A Powerful Weapon in the Arsenal for Environmental Control," *The Photonics Design and Applications Handbook*: H-309-318 (1994).

3.   U.S.A.F. Fact Sheet, "Laser Medical Pac," (January 1994).

4.   Schwartz, William. "Solid-state Lasers Point to the Future in Military Applications," *Laser Focus World*: 75-96 (July 1991).

5.   Hecht, Jeff. "Gallium Arsenide Lasers Offer an array of Options," *Laser Focus World*: 83-92 (July 1993).

6.   Baumann, Melissa G. D. *et al.* "Diode Lasers," *Journal of Chemical Education,* 69: 89-95 (February 1992).

7.   Byer, Robert L. "Diode Laser-pumped Solid-state Lasers," *Science*, 239: 742-747 (February 1988).

8.   Williams, M. D. "Laser Power Beams Obtained by the Dynamic Selection of Emitting Elements in an Array," *Applied Optics*, 31 (15): 2738-2742 (May 1992).

9.   Hillman, Paul D. and M. Marciniak. "Phase locking Laser Diodes Using Photorefractive Coupling," *Journal of Applied Physics*, 66 (12): 5731-5737 (December 1989).

10.   Verdeyen, Joseph T. *Laser Electronics* (Second Edition). Englewood Cliffs, NJ: Prentice-Hall, 1989.

11.   Cross, Peter S. *et al.* "Ultrahigh-power Semiconductor Diode Laser Arrays," *Science*, 237: 1305-1309 (September 1987).

12.   Spectra Diode Labs. *Laser Diode Operator's Manual & Technical Notes.* Product Brochure. San Jose, CA: October 1991.

13. Botez, D. and D. E. Ackley. "Phase-Locked Arrays of Semiconductor Diode Lasers," *IEEE Circuits and Devices Magazine*, 23 (1): 8-17 (1986).

14. Streifer, W. *et al.* "Phased Array Diode Lasers," *Laser Focus/Electro-Optics*: 100-107 (June 1984).

15. Thaniyavarn, S. and W. Dougherty. "Generation of a Single-Lobed Radiation Pattern from a Phased-array Laser Using a Near-contact Variable Phase-shift Zone Plate," *Applied Physics Letters*, 50: 1541-1543 (1987).

16. Ackley, D. E., D. Botez, and B. Bogner. "Phase-locked Injection Laser Arrays with Integrated Phase Shifters," *RCA Review*, 44: 625 (1983).

17. Matsumoto, M., M. Taneya, S. Matsui, S. Yano, and T. Hijikata. "Single-lobed Far-field Pattern Operation in a Phased Array with an Integrated Phase Shifter," *Applied Physics Letters*, 50 (22): 1541-1543 (1987).

18. Itoh, H. *et al.* "Fringe Shifting of Phase-coupled Array Lasers for Optical Logic Operations," *International Journal of Optical Computing*, 2: 89-96 (1991).

19. Kenyon, Greg S. *Characterization of an LCD for Use as a Programmable Phase Shifter to Produce a Single-lobed Far-field Pattern in a Phased Array*. MS thesis, AFIT/GAP/ENP/93-D-05. School of Engineering, Air Force Institute of Technology (AU), Wright-Patterson AFB OH, December 1993 (AAK7853).

20. Welch, D. F. *et al.* "High-power (575mW) Single-lobed Emission from a Phased-array Laser," *Electronics Letters*, 21 (14): 603-605 (July 1985).

21. D'Amato, F. X., E. T. Siebert, and C. Roychoudhuri. "Coherent Operation of an Array of Diode Lasers Using a Spatial Filter in a Talbot Cavity," *Applied Physics Letters*, 55 (9): 816-818 (August 1989).

22. Leger, James R., M. L. Scott, and W. B. Veldkamp. "Coherent Addition of AlGaAs Lasers Using Microlenses and Diffractive Coupling," *Applied Physics Letters*, 52 (21): 1771-1773 (May 1988).

23. Chaing-Hasnain, C. J. *et al.* "High Power with High Efficiency in a Narrow Single-lobed Beam from a Diode Laser Array in an External Cavity," *Applied Physics Letters*, 50 (21): 1465-1467 (1987).

24. Goldberg, L. and J. F. Weller. "Narrow Lobe Emission of High Power Broad Stripe Laser in External Resonator Cavity," *Electronics Letters*, 25 (2): 111-113 (January 1989).

25. MacCormack and J. W. Eason. "Near-diffraction-limited Single Lobe Emission from a High-power Diode-laser Array Coupled to a Photorefractive Self-pumped Phase Conjugate Mirror," *Optics Letters*, 16: 705-707 (1991).

26. Tatsuno, K. *et al.* "Diffraction-limited Circular Single Spot from Phased Array Lasers," *Applied Optics*, 28: 4560-4568 (1989).

27. Weber, J. *Lasers*. New York, NY: Gordon and Breach Science Publishers, 1968.

28. Neumark, G. F., R. M. Park, J. M. DePuydt. "Blue-green Diode Lasers," *Physics Today*: 26-32 (June 1994).

29. Lacy, Edward A. *Fiber Optics*. Englewood Cliffs, NJ: Prentice-Hall, 1982.

30. Ripper, J. E. and T. L. Paoli. "Optical Coupling of Adjacent Stripe Geometry Junction Lasers," *Applied Physics Letters*, 17: 371-373 (1970).

31. Spencer, M. B. and W. E. Lamb, Jr. "Theory of Two Coupled Lasers," *Physics Review A*, 5 (2): 893-898 (1972).

32. Scifres, D. R., R. D. Burnham, and W. Streifer. "Phase Locked Semiconductor Laser Array," *Applied Physics Letters*, 33: 1015-1017 (1978).

33. Paoli, T. L., W. Streifer, and R.D. Burnham. "Observation of Supermodes in a Phase-locked Diode Laser Array," *Applied Physics Letters*, 45: 217-219 (August 1984).

34. Epler, J. E. *et al.* "Far-field Supermode Patterns of a Multi-stripe Quantum Well Heterostructure Laser Operated in an External Grating Cavity," *Applied Physics Letters*, 45: 406-408 (August 1984).

35. Temkin, H. *et al.* "Index-Guided Arrays of Schottky Barrier Confined Lasers," *Applied Physics Letters*, 46 (5): 465-467 (March 1985).

36. Butler, J. K., D. E. Ackley, and D. Botez. "Coupled-mode Analysis of Phase-locked Injection Laser Arrays," *Technical Digest of the Optical Fiber Communication Conference*, Paper TuF2, 44-46. New Orleans, LA: January 23-25, 1984.

37. Butler, J. K., D. E. Ackley, and D. Botez. "Coupled Mode Analysis of Phase-Locked Injection Laser Arrays," *Applied Physics Letters*, 44: 293-295 (February 1984).

38. Segev, M. and B. Fischer. "Laser Diode Arrays with Apertured Phase Conjugate Feedback," *IEEE Journal of Quantum Electronics*, 26 (8): 1318-1322 (August 1990).

39. Scifres, D. R., W. Streifer, and R. D. Burnham. "Experimental and Analytic Studies of Coupled Multiple Stripe Diode Lasers," *IEEE Journal of Quantum Electronics*, QE-15: 917-922 (September 1979).

40. Goodman, J. W. *Introduction to Fourier Optics*. San Francisco, CA: McGraw-Hill, 1968.

41. Hecht, Eugene. *Optics* (Second Edition). Reading, MA: Addison-Wesley Publishing Company, 1990.

42. Sirohi, R. S. *A Course of Experiments with He-Ne Laser*. New York, NY: Halsted Press, 1985.

43. Born, Max and E. Wolf. *Principles of Optics*. New York, NY: Pergamon Press, 1965.

44. The Ealing Corporation. *Universal Interferometer An Experimental Handbook*. South Natick, MA: The Ealing Corporation, 1979.

45. Pressley, Robert J., ed. *CRC Handbook of Lasers*. Cleveland, OH: Chemical Rubber Company, 1971.

46. Grantham, Jeffrey W. Assistant Professor of Physics, Department of Engineering Physics, Air Force Institute of Technology, Wright-Patterson AFB, OH. Personal interview. 1 Aug 94.

47. Gaskill, Jack D. *Linear Systems, Fourier Transforms, and Optics*. New York, NY: John Wiley & Sons, 1978.

Vita

Captain Thomas A. Summers was born on 17 March 1963 in Portsmouth, Virginia. In 1965 he and his family moved to Rochester, Pennsylvania where he graduated from Quigley High School in May, 1981. He attended Saint Vincent College in Latrobe, Pennsylvania and graduated with a Bachelor of Science degree in Physics in May, 1985. After graduation he worked at Argonne National Laboratory in Argonne, Illinois and Los Alamos National Laboratory in Los Alamos, New Mexico. He received a reserve commission in the United States Air Force from Officer Training School and served his first tour of duty as a missile launch officer at Minot AFB, North Dakota. In May, 1993 he entered the School of Engineering, Air Force Institute of Technology where he will graduate in December, 1994 with a Master of Science in Engineering Physics. His follow-on assignment is to the United States Air Force Academy in Colorado Springs, Colorado as a physics instructor.

Permanent Address: 218 Greenwood Drive
New Brighton, PA 15066